Breathing and moving vesicles in a geometric mechanochemical model

Alexander Meiners, Hannes Uecker

Institut für Mathematik, Universität Oldenburg, D26111 Oldenburg, alexander.meiners@uni-oldenburg.de, hannes.uecker@uni-oldenburg.de

June 27, 2026

Abstract

We consider a geometric mechanochemical model of vesicles which couples the Helfrich flow for the shape of a lipid bilayer vesicle membrane X with a reaction-diffusion equations for a single "morphogen" ϕ on X. The Helfrich flow is the L^2 gradient flow of the elastic bending energy $E(X) = \int_X (H - c_0)^2 dS$ of X, typically supplemented by area or volume constraints, or both. The morphogen ϕ adsorbs/desorbs at places of high/low mean curvature H, i.e., the kinetics of ϕ depend on H, and conversely ϕ modifies the spontaneous curvature c_0 on X. The flow is no longer gradient, and hence allows for more complicated dynamics, including time periodic orbits, e.g., "breathing and moving" vesicle shapes. We show how to compute bifurcation diagrams for such solution branches via numerical continuation and bifurcation methods. We mostly focus on "planar" vesicles (1D closed curves) but also give an outlook on 3D vesicles (2D closed membranes).

Contents

1 Introduction

Oscillations of biological membranes are an important building block of cell biology, and have been presented in the setting of giant unilamellar vesicles (GUVs) and other synthetic biomimetic vesicles in a number of recent studies [TUSY14, LRM$^+$18, MSD18, SZHZ20, LDS20, LMFAO21, TN22, Lip22, Nog25]. For instance, [LRM$^+$18] reports experiments with GUVs that enclose a fluid with Min proteins that show some time periodic dynamics, and can change the spontaneous (or preferred) curvature c_0 of the membrane by adsorption to or desorption from the membrane. The membrane oscillations then found include "pulsing", where the MinD periodically in time but uniformly in space adsorbs/desorbs to/from the membrane, "Pole–to–Pole oscillations" where MinD periodically switches between two spherical caps, "circling", and "trigger waves", see Fig.1. In all these, some area *and* volume changes of the vesicles seem involved, but no significant shape changes as the vesicles always stay essentially spherical. On the other hand, rather drastic shape (and topology) changes can also occur, for instance periodic closing and opening of necks of dumbbell shaped vesicles, and is explained by the phase diagrams of stable vesicle shapes from [SBL90] depending on the spontaneous curvature c_0 of the Helfrich energy $\mathcal{H}$ (see (1)), namely that the periodic dumbbell dynamics follow the instantaneous minimizers of $\mathcal{H}$ at the given $c_0(t)$.

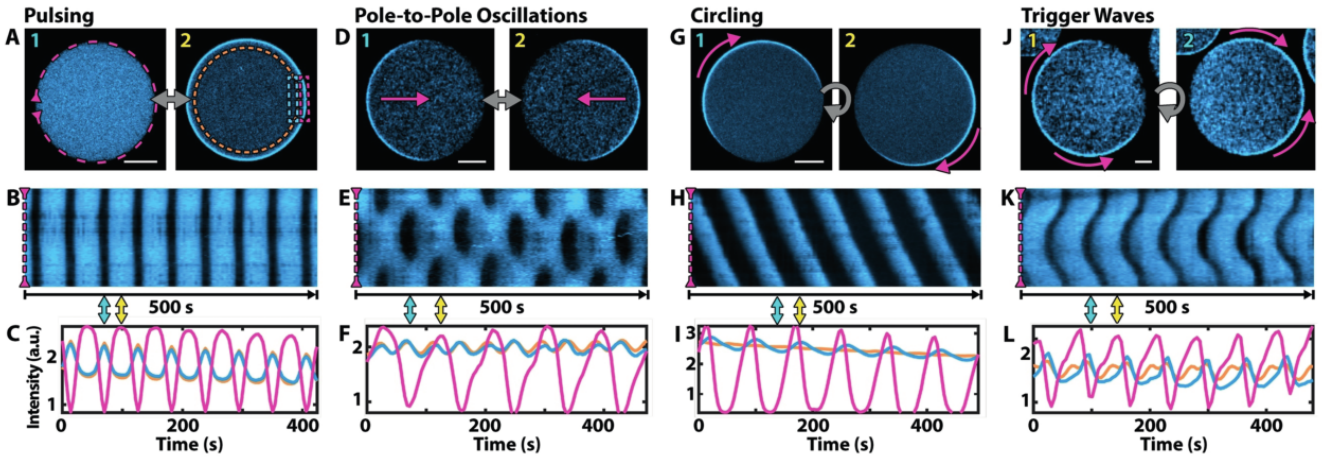

Figure 1: Experiments from [LRM$^+$18]. The top rows show snapshots of Min intensities, with the magenta arrows indicating the directions of waves. The kymographs and time series in the center and bottom rows, are (normalized) intensities from the magenta and blue boxes in A, and the orange curve is the average intensity in the vesicle.

A classical geometric model of closed vesicle lipid bilayer membranes X is the Canham–Helfrich energy [Hel73]

$$\mathcal{H}(X, c_0) = \int_X (H - c_0)^2 \, \mathrm{d}S, \tag{1}$$

where $H = \frac{1}{2}(\kappa_1 + \kappa_2)$ is the mean curvature of X, i.e., the mean of the two principal curvatures on X, and the parameter $c_0 \in \mathbb{R}$ is called the spontaneous curvature and depends on the properties of the lipid bilayers forming the membrane, and on the properties of the fluid in which the vesicles form. Stable vesicle shapes are obtained from minimizing $\mathcal{H}$ under fixed enclosed volume $\mathcal{V}$ and surface area $\mathcal{A}$, and the associated Euler–Lagrange equation is called the Helfrich equation. See, e.g., [SBL90, SL95, Sei97] for detailed 2–parameter (c_0, and reduced volume $v = \mathcal{V}/\mathcal{A}$) phase diagrams of axisymmetric vesicles obtained from (numerical) solution of the Helfrich equation, and [MU24b, §4.1] for further continuation and bifurcation results, including non–axisymmetric shapes.

The L^2 gradient flow associated to $\mathcal{H}$ is called the Helfrich flow, and is studied from a mathematical perspective in, e.g., [NY12, RSS24] for closed vesicles, and in [MU26a] for periodic cylinders, which show wrinkling, pearling and coiling as primary instabilities of straight cylinders. However, as $\mathcal{H}$ is

non–increasing in these gradient flows, and in fact decreasing except in steady state, these models do not allow time-periodic solutions. To model time periodic behavior as in Fig.1, a natural idea is to combine the gradient dynamics for $\mathcal{H}$ with chemistry, yielding so called mechanochemical models, which come in at least two ways.

- Bulk–surface coupling: In these, the dynamics of some chemicals in the fluid (the bulk) is coupled to the interaction of the chemicals with the membrane (the surface). The dynamics in the bulk may be of simple linear diffusion type. For instance, [SG11] finds oscillations in a system of a fluid layer between two membranes which are graphs over a plane, where neither the bulk (linear diffusion) nor the membranes alone would generate oscillations. See also [GMGOS07] for a somewhat simplified system without membrane shape changes, with a detailed analysis in [GW16], which is extended in [PLXD$^+$20]. On the other hand, in [LRM$^+$18, CLSL21] it is argued that for the experiments shown in Fig. 1 the situation is rather the converse, at least in A–C: There is a time periodic reaction and fast diffusion of the Min proteins in the bulk, thus yielding an effective spatially homogeneous time-periodic forcing via $c_0(t)$ on the membrane.
- Reaction–diffusion (RD) systems on the membrane X: Here, some chemicals can adsorb/desorb from the fluid to X and react and diffuse there, but the dynamics in the fluid are not modeled. The reaction on X, or in particular the adsorption/desorption, depends on the (mean) curvature H of X, and vice versa the chemicals influence the spontaneous curvature c_0 on X. A simple phenomenological model for this, with just one abstract chemical species ϕ (a morphogen), is set up and analyzed numerically in [MHMC13, MMCRH13], see also [BMRMC18]. Relatedly, in [TN20, TN21], the Helfrich flow for X is coupled to a Brusselator type RD system for two chemical species v_1 and v_2 on X with dynamics depending on H, see also [Nog25].

Both classes of models come with different constraints, i.e., fixed membrane area, or fixed enclosed volume, or both. In any case, in both classes, the full dynamics are in general no longer of gradient type, and hence allow for time–periodic behavior.[1]

A 1D version (without area or volume constraints) of coupling of Helfrich energy with branched c_h vs bundled c_v actin on membranes is treated in [IMK$^+$13], yielding a 4th order Helfrich type equation for the membrane height h coupled to a two component RD system for (c_h, c_v). Additionally, somewhat phenomenological 1D models without genuine geometry are treated in [YFB22, BEGY23, HMTB$^+$25], i.e., reaction–diffusion models for F–actin, and active and inactive forms of GTPase, but without membrane mechanics. Under the crucial ingredient of conservation of the total GTPase mass, the models show bistability of "wave–pinning" (steady patterns), traveling waves, and standing oscillations, which are moreover related to experimental results for *D. discoideum* cells.

From the diverse possible mechanochemical models, and although the motivating experimental results from Fig.1 rather come from the bulk–surface class, here we analyze models based on [MHMC13, MMCRH13] via numerical bifurcation and continuation, following our previous work [MU24b, MU26a]. For closed 2D membranes, the model reads

$$\partial_t X = -[\Delta(H - c_0) + 2H(H^2 - K) + 2c_0 K - 2c_0^2 H + \lambda H]N, \tag{2a}$$

$$\partial_t \phi = D\Delta\phi - \delta\phi + g(H). \tag{2b}$$

In the Helfrich flow (2a) of X, again H is the mean curvature (always wrt to the inner normal N of X, i.e., $H = 1/R$ for a sphere of radius R), K is the Gaussian curvature, Δ is the Laplace–Beltrami

[1] There are also membrane models based on the Koiter elasticity model coupled to reaction–diffusion of chemicals in the surrounding (or enclosed) medium. For instance, in [MSD18] a Koiter elastic energy is coupled to a FitzHugh–Nagumo model, while [LDS20] considers disk–shaped Belousov–Zhabotinsky (BZ) gels in a BZ solution, and the periodic BZ reaction drives a swelling of the gel which alters its mechanical properties and hence yields periodic buckling, and a similar setup is considered in [LMFAO21], with a Helfrich term included in the elastic energy. In all three models, time–periodic shapes changes of the membranes and periodic waves on the membranes are observed, which inter–alia may yield locomotion of the vesicles.

operator on X, and the spontaneous curvature

$$c_0 = c_0(\phi) = \alpha + \beta\phi \tag{2c}$$

depends on ϕ via parameters $\alpha, \beta \in \mathbb{R}$. The morphogen ϕ diffuses with rate $D > 0$ on X and decays with rate $\delta > 0$, and H influences the dynamics of ϕ via the function

$$g(H) = \zeta \frac{f(H)}{\omega + f(H)}, \tag{2d}$$

with coupling constant $\zeta \in \mathbb{R}$ and parameter $\omega > 0$, and where $f(H)$ is a smoothed version of $\max(0, H - H_n)$ for some normalization $H_n > 0$, e.g., $H_n = 1/R$ for a sphere of radius R. The morphogen is thus "generated" (i.e., adsorbs) at places of higher H. Different from [MU24b, MU26a], and as in [MHMC13, MMCRH13] we do not fix the enclosed volume which can adapt via osmosis, but the membrane X is still inextensible, and λ is a Lagrange multiplier for the area constraint[2]

$$q(X) = A(X) - A_0 = 0. \tag{2e}$$

However, for numerical efficiency and simplicity, see Remark 1.1, we first consider 1D membranes (curves) γ. For these, the mean curvature H of (2) is replaced by the curvature κ, hence $\mathcal{H}(\gamma, c_0) = \int_\gamma (\kappa - c_0)^2 \, \mathrm{d}s$, and the model reads

$$\partial_t \gamma = -[\Delta(\kappa - c_0) + \frac{1}{2}\kappa(\kappa + c_0)(\kappa - c_0) + \lambda\kappa]\nu, \tag{3a}$$

$$\partial_t \varphi = D\Delta\varphi - \delta\varphi + \zeta \frac{f(\kappa)}{\omega + f(\kappa)}, \tag{3b}$$

where ν is the (inner) normal to the curve, together with the length constraint $q(\gamma) := L(\gamma) - L_0$, which determines the Lagrange multiplier λ, where wlog $L_0 = 2\pi$.

Figure 2(a,b) gives a preview of 1D results, and (c) just one typical 2D time periodic orbit (PO). In both, 1D and 2D, we essentially fix the parameters $(\beta, \omega, \delta, D)$, and for different choices of α compute bifurcation diagrams of steady states and POs with the coupling constant ζ as the primary active bifurcation parameter. In a nutshell, in 1D, the circle $\mathbb{S}^1$ with $\phi \equiv 0$ is always a steady state for (3) (via $2\lambda = c_0^2 - \kappa^2$) for the given parameters. This yields a "trivial" solution branch, but as the coupling constant ζ increases beyond some critical value, $\mathbb{S}^1$ looses stability and first some nontrivial branches of D_m symmetrical shapes bifurcate, see (a) for a D_4 symmetric sample. Then, POs may bifurcate from the D_m symmetric shapes, sample in (b). The stability of these is difficult to assess from their Floquet multipliers, due to always present neutral translational and rotational modes, and hence we supplement the bifurcation analysis by some direct numerical simulation (DNS), see also Remark 1.1b). In these, the D_4 symmetric PO E (with kymographs like in Fig.1E) turns out to be metastable in DNS in the labframe, and after some transient the solutions turns into "trigger waves" like in Fig.1K, in with the vesicle additionally starts to tumble. However, if we integrate (3) in a comoving frame, i.e., trade spatial translations for positional Lagrange multipliers, see Remark 1.1b), then the PO E is stable. Similar behavior is presented for 2D vesicles in §3, cf. Fig. 2(c).

Importantly, while Fig.2 only previews samples (steady states and POs), in §2 and §3 we give full bifurcation diagrams of branches of such states.

[2]Instead of the global area constraint $A(X) - A_0 = 0$, [MMCRH13, MMCRH13] assume a local inextensibility and consequently introduce a field λ on X and allow tangential motion of X, while here we restrict to normal motion only. The equivalence of both approaches for steady states of Helfrich flows of genus 0 surfaces (conformally equivalent to the sphere) is shown in [DH15]. For the genuine dynamical problem (2) the physical argument for using just a number λ is that the surface tension always relaxes so fast that it is effectively homogeneous and isotropic on X, cf.[GNPS96]. Nevertheless, here this is a modeling choice/assumption.

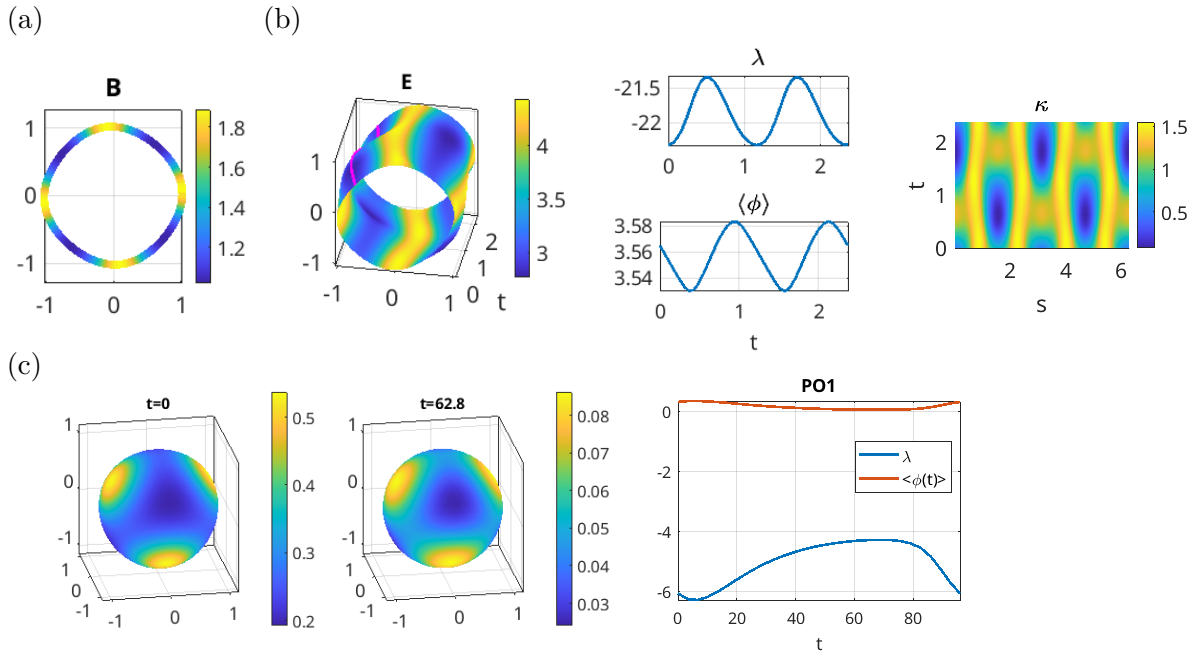

Figure 2: Preview: (a) steady D_4 symmetric 1D vesicle, colored by ϕ; $(\alpha,\beta,\delta,D,\omega)$=$(0.7,1,0.3,0.1,1)$, $\zeta\approx 5.67$. (b) breathing D_4–symmetric 1D vesicle (bifurcating from B), $\zeta\approx 8.13$. Left: shape as a function of t; the red line indicates the arclength $s=0$ section. Middle: time series of λ and the average coverage $\langle\phi(t)\rangle := \frac{1}{2\pi}\int_0^{2\pi}\phi(s,t)\,\mathrm{d}s$. Right: kymograph of κ. (c) Sample of a breathing 2D vesicle with tetrahedral symmetry, $(\alpha,\beta,\delta,D,\omega)=(2,1,0.1,0.1,1)$, $\zeta\approx 3.45$.

Remark 1.1. a) The numerics are naturally much less expensive in 1D than in 2D; this is in particular important for POs, i.e., (1+1)D vs (2+1)D. Equally important, the 1D problem is much easier from a symmetry point of view. In 1D, the symmetry group of the primary bifurcations from the circle $\mathbb{S}^1$ is $O(2)$, the linearization can be analyzed by Fourier modes, and the kernels are generically 2-dimensional. In 2D, we have $O(3)$ equivariant bifurcations from the sphere, with high–dimensional kernels given by spherical harmonics, cf.[Mat04].

b) Due to the length constraint $q(\gamma)=0$, (3) (resp. (2) with area constraint $q(X)=0$ in 2D) always is a (partial) differential algebraic equation DAEs of (differentiation) index 2; moreover for continuation of steady states and POs, and also for DNS, we shall need additional positional constraints (aka phase conditions), yielding further index 2 components for the DAE system. In a simple setting, we then use an implicit Euler scheme for the DNS of these DAEs, which however we also cross–check with DNS based on the high–order and adaptive code `RADAU` [HLR89][3], yielding essentially the same results. See also App.B.1. ⌋

Remark 1.2. a) Given a base manifold X_0, and setting $X=X_0+uN$ with normal N and normal displacement u, we can write (2a), and the analogous version in 1D, as 4th order equations for u. In [MMCRH13, MHMC13] this mechanochemical model is then related to 2–component activator–inhibitor RD systems as follows: u is a fast long–range (4th order) activator, while ϕ (with typically small $D>0$) is a slow short-range inhibitor. In this sense, one chemical species (the morphogen ϕ) coupled to curvature is sufficient to obtain (tuneable, see b)) pattern formation, and no genuine RD *systems* on X are needed. However, this is also related to the important length (1D) resp. area (2D) constraints: Without these, i.e., without λ in (3a), circular vesicles can just grow in radius and no patterns develop, and the same holds in 2D for growing spheres. The fast–slow point of view (small $D>0$, compared to fast relaxation of the membrane) is further pursued in the setting of (3) in [NDV25] as fast–slow dynamics in space to study pattern formation via geometric singular perturbation theory.

[3]with code available at `https://www.unige.ch/~hairer/software.html`

b) By "tuneable" in a) we mean that by adapting the chemical parameters β, D, δ and ω (with ζ used as the continuation parameter) we can choose the wave-number $m\in\mathbb{N}$ (in 2D the spherical harmonic number l) at which under continuation in ζ the circle (the sphere) first becomes unstable, where we then expect bifurcation of stable patterns with wave number m (spherical harmonic number l). In the purely mechanical Helfrich model, the first bifurcation is always with $m = 2$ (resp. $l = 2$ in 2D, i.e., prolates and oblates). ⌋

The rest of the paper is structured as follows. In §2 we explain the 1D model (3), including the precise form of $f(\kappa)$, and discuss the linearization at the circle. We then present detailed BDs for this 1D model, and in §3 similar results in 2D, and in §4 we end with a discussion and outlook. In App.A we collect some results from differential geometry, discuss the setting of the phase conditions, and briefly the amplitude formalism to describe the steady bifurcations from the circle; this reflects the particular choice how we approximate the non–smooth function $f(\kappa) = \max(0, \kappa-\kappa_n)$ of the original model by the smoothed versions $f_\chi(\kappa)$ (see (5)). In App.B we comment on the numerical methods, in particular on the extension of the `Xcont` setting of `pde2path` to PO problems, the mesh–handling, and the DNS methods for the DAEs.

Table 1: Acronyms.

Acronym	**Meaning**	**Acronym**	**Meaning**
AE	amplitude equation	BD	bifurcation diagram
BP, HP	branch point, Hopf point	DAE	differential algebraic equation
DNS	direct numerical simulation	cDNS	constrained DNS
IC	initial condition	PO	(time-)periodic orbit
COM	center of mass	RD	reaction diffusion

Notation. Table 1 summarizes the acronyms used in the paper. Additionally, by D_m we denote the dihedral group of order m, i.e., the symmetry group of a regular m–gon, generated by rotation with angle $2\pi/m$ and one reflection, important for the symmetry considerations of bifurcations in the 1D model.

2 The 1D model

For the 1D version (3) of (2), let

$$\mathcal{H}(\gamma, c_0) = \int_\gamma (\kappa - c_0)^2 \, \mathrm{d}s, \tag{4}$$

be the bending energy of a (closed) curve $\gamma \in \mathbb{R}^2$ with curvature κ, where again $c_0 \in \mathbb{R}$ is a spontaneous curvature, which we take to depend on a morphogen ϕ via (2c), i.e., $c_0{=}c_0(\phi){:=}\alpha{+}\beta\phi$ with parameters $\alpha{\in}\mathbb{R}$ and $\beta > 0$. The gradient flow of (4) with respect to the L^2 inner product, $\langle f, g\rangle_{L^2} := \int_\gamma \langle f, g\rangle_{\mathbb{R}^2} \, \mathrm{d}s$, under the length constraint $L(\gamma) = L_0$, and coupled with the morphogen dynamics yields (3), which below we express in local coordinates.

The original model uses $f(\kappa) = \max(0, \kappa - \kappa_0)$ with κ_0 a reference curvature, e.g., $\kappa_0 = 1/R$ for a circle of radius R. However, this is not differentiable at $\kappa = \kappa_0$, and therefore we replace it with the smooth approximation $f(\kappa) := \dfrac{1}{\chi} \log\left(\left(e^{\chi(\kappa-\kappa_0)} + 1\right)\right.$ which converges to $\max\{\kappa - \kappa_0, 0\}$ as $\chi \to \infty$, uniformly for $\kappa \in \mathbb{R}$. For convenience (i.e., to have the trivial branch $(\kappa, 0) = (\kappa_0, 0)$ independent of further parameters) we subtract $\log(2)/\chi$ from $f(\kappa)$, i.e., finally choose

$$f(\kappa) := \frac{1}{\chi}\left(\log\left(e^{\chi(\kappa-\kappa_0)} + 1\right) - \log(2)\right), \tag{5}$$

and generally fix $\chi = 50$, see Fig.14 in App.A.3 for sketches. We then have 8 parameters ($L, \kappa_0, \alpha, \beta, D, \delta, \zeta, \omega$), but by scaling we can reduce to $L = 2\pi$, $\kappa_0 = 1$, i.e.: The elastic energy satisfies $\mathcal{H}(\varepsilon_\gamma \gamma, c_0) = \mathcal{H}(\gamma, \varepsilon_\gamma^{-1} c_0)$ for any $\varepsilon_\gamma > 0$; hence (3a) shares this property. In particular, the case $c_0 = 0$ (Willmore energy) is scale-invariant. Thus, we can fix the scale by choosing $L = 2\pi, \kappa_0 = 1$, and adapting α, β. Here we restrict ourselves to the case of fixed $(\beta, \omega) = (1, 1)$, and $(D, \delta) = (0.1, 0.3)$, as the dynamics of ϕ is considered to be slower than that of γ, and will look at different values of α, while the coupling constant ζ will be our primary continuation parameter.

Remark 2.1. The smoothness of f from (5) is needed for standard local stability and bifurcation analysis of $\mathbb{S}^1$, and similarly at the sphere in 2D. We have $f'(\kappa_0)=1/2$ independent of χ, but $f''(\kappa_0)=\chi/4$ and $f^{(n)}(\kappa_0)=\mathcal{O}(\chi^{n-1})$. Thus, the linear stability of $\mathbb{S}^1$ (with $\kappa_0=1$) does not depend on χ, but the higher order terms in the local bifurcation analysis for (3) at BPs from $\mathbb{S}^1$ strongly depend on χ. In particular, the validity range of the amplitude equations for the bifurcations shrinks with increasing χ, see §A. Thus, the choice of χ is a modeling decision and we took χ=50 to be close to the original model. ⌋

2.1 Local coordinates, local existence, and linear stability analysis at the circle

Let $\gamma : [0, 2\pi) \to \mathbb{R}^2$ be a smooth, parameterized, inward-oriented closed curve, and let τ and ν denote the unit tangent and normal vector fields along γ, defined by

$$\tau = \frac{\gamma_s}{\|\gamma_s\|_2}, \quad \nu = \frac{\tau_s}{\|\tau_s\|_2}, \tag{6}$$

where $\gamma_s = \partial_s \gamma$. We denote the metric by $g = \|\gamma_s\|_2^2$, and the Laplace–Beltrami operator on γ by Δ, with $\Delta u = g^{-1}\partial_s \left(g^{-1}\partial_s u\right)$, and then have

$$\kappa = \langle \Delta\gamma, \nu \rangle \tag{7}$$

for the curvature κ.

To evaluate (3a), the authors of [MMCRH13] consider variations of the form $\gamma + u\,N + \psi\,T$, involving both the normal component u and the tangential component ψ. Here, wlog (see [KPP17]) we restrict to normal variations. If we write $\gamma_\eta = \gamma + \eta u \nu$, and with a slight abuse of notation let $L(\eta) = L(\gamma_\eta)$, then $L'(0) = -\int \kappa u \,\mathrm{d}s$. Therefore, (3a) becomes

$$\langle \partial_t \gamma, \nu \rangle = -\Big(\partial_u \mathcal{H} - \lambda(u)\kappa \Big), \quad \partial_u \mathcal{H} = \Delta(\kappa - c_0) + \frac{1}{2}\kappa(\kappa + c_0)(\kappa - c_0), \tag{8}$$

and where $\lambda(u) = -(\int_\gamma \kappa^2 \,\mathrm{d}s)^{-1} \int_\gamma \kappa \partial_\gamma \mathcal{H} \,\mathrm{d}s$ is a non-local term obtained from $0 = \frac{\mathrm{d}}{\mathrm{d}t} q(\gamma) = \partial_\gamma L(\gamma)[\partial_t \gamma]$. The notation $\lambda(u)$ in (8) thus means that we consider the Helfrich flow projected on the constraint $L(\gamma) = L_0$.

The trivial steady state solution is the circle $\mathbb{S}^1$, with $2\lambda = c_0^2 - \kappa^2$ for any $c_0 \in \mathbb{R}$. We fix the arc-length parametrization of $\mathbb{S}^1$ so that $\kappa = 1$, i.e., $s \mapsto (\cos(s), \sin(s))^T$ and $\nu_0 = -(\cos(s), \sin(s))^T$, and let

$$\gamma = \mathbb{S}^1 - u\nu_0, \tag{9}$$

where we chose $-u$ instead of $+u$ as the formulas become slightly nicer. We rewrite (8) for a normal variation u of $\mathbb{S}^1$ with the metric

$$g(u) = (1 + u)^2 + u_s^2, \tag{10}$$

and the curvature

$$\kappa(u) = \frac{1}{g^{1/2}(u)} - \frac{(1+u)}{g^{3/2}(u)} u_{ss}, \tag{11}$$

and obtain

$$\begin{pmatrix} \frac{1+u}{g^{1/2}(u)} & 0 \\ 0 & 1 \end{pmatrix} \begin{pmatrix} u_t \\ \varphi_t \end{pmatrix} = \mathcal{G}(u,\varphi) = \begin{pmatrix} -\big(\Delta(\kappa - c_0) + \frac{1}{2}\kappa\big(\kappa + c_0\big)\big(\kappa - c_0\big) - \lambda(u)\kappa\big) \\ D\Delta\varphi - \delta(\varphi - \varphi_0) + \zeta f_m(\kappa)(\omega + f_m(\kappa))^{-1} \end{pmatrix}. \tag{12}$$

Following [MU26a], we define

$$V_\epsilon^\theta = H^\theta(\mathbb{S}^1) \cap \{u : \, L(\mathbb{S}^1 - u\nu) = 2\pi\} \cap \{u \geq -1 + \epsilon\},$$

for $\theta > 5/2$ (not a half-integer) and $0 < \epsilon < 1$. Then V_ϵ^θ is non-empty (spanned by Fourier modes with wave number $m \in \mathbb{Z} \setminus \{0\}$ from the length constraint), and (12) is parabolic and possesses the maximal regularity property on $V_\varepsilon^\theta \otimes H^1(\mathbb{S}^1)$ as a closed subset of $L^2(\mathbb{S}^1) \otimes L^2(\mathbb{S}^1)$. From this we obtain we obtain local existence for (12) for initial conditions $(u_0, \phi_0) \in (V_\varepsilon \otimes H^1)$, cf. [MU26a], with simple modifications to account for the $\partial_t\phi$ equation.[4] However, we have no general results on global existence.

For the numerical algorithms, it is helpful to also implement the Jacobian $\partial_{(u,\phi)}\mathcal{G}$ at a general γ, see Appendix A for the derivation, but here we first explicitly linearize at $\mathbb{S}^1$, i.e., at the homogeneous steady state $\big(u_h, \varphi_h\big) = \big(0, 0\big)$, with $\lambda(0) = \frac{1}{2}(c_0^2 - 1)$. For normal variations of $\mathbb{S}^1$, the linearization of (3) reads

$$\begin{pmatrix} 1 & 0 \\ 0 & 1 \end{pmatrix} U_t = \mathcal{L}(\partial_s, \Lambda)U, \tag{13}$$

where Λ stands for the parameters $(D, \delta, \beta, \omega, \alpha, \zeta)$. This is a linear parabolic system with constant coefficients and hence has solutions of the form

$$U(x,t) = \exp(t\mu_m + \mathrm{i}ms)\Phi_m \tag{14}$$

for wave numbers $m \in \mathbb{Z} \setminus \{0\}$ (0 excluded due the length constraint), where $(\mu_m, \Phi_m) \in \mathbb{C} \times \mathbb{C}^2$ is an eigenpair of the Fourier-transformed linearization

$$\mathcal{L}(\mathrm{i}m, \Lambda) = \begin{pmatrix} -(m-1)^2(m+1)^2 & \beta(m^2 - \alpha) \\ \frac{\zeta}{2\omega}(m^2 - 1) & -Dm^2 - \delta \end{pmatrix}. \tag{15}$$

Due to $\int_\gamma e^{ims} \, \mathrm{d}s = 0$ for $m \neq 0$ we have $\partial_u \lambda(u)|_{u=0} = 0$ such that the constraint is absent in (15). For $m = 1$, we have two zero eigenvalues related to rigid body motions, which we will remove via phase conditions, see App.A.2. Also note that $\partial_u \mathcal{G}_1$ is independent of any parameter; hence, $\mathbb{S}^1$ is stable without morphogen coupling. This is different from the work in [MU26a], where the presence of pressure destabilizes the circle (treated as a cylinder in [MU26a]). See §2.2.1 for a review of this case.

By analyzing the dispersion relation $m \mapsto \mu_m(\Lambda)$ for (15), we find that an easy way to control the wave number of the primary instability is by varying the spontaneous curvature α. Namely, given a wave number m, solving $\mu(m, \Lambda) = 0$ for the critical value of our bifurcation parameter ζ we obtain

$$\zeta_c(m) = \frac{2\omega(m-1)(m+1)(Dm^2 + \delta)}{(m^2 - \alpha)\beta}, \tag{16}$$

which for instance gives the plots in Fig.3(a), with subsequent plots of the eigenvalues at the marked points. Of course, there are other possibilities to manipulate the ζ_c (in particular, $\zeta_c(m)$ is a decreasing function of ω, D, and δ, but (16) and Fig.3(a) show that, e.g., for fixed $(\alpha, \delta) = (0.7, 0.3)$ (and always $(\beta, \omega, D) = (1, 1, 0.1)$ fixed), increasing ζ from $\zeta < \zeta_c$ the first bifurcation is to $m = 2$, the second to $m = 3$, and so on. On the other hand, for $\alpha = 3$, the order is $m = 3, 2, 4, \ldots$, and for instance

[4] This works fully analogous near the sphere in 2D, with the only difference that $\theta > 3$ is needed then.

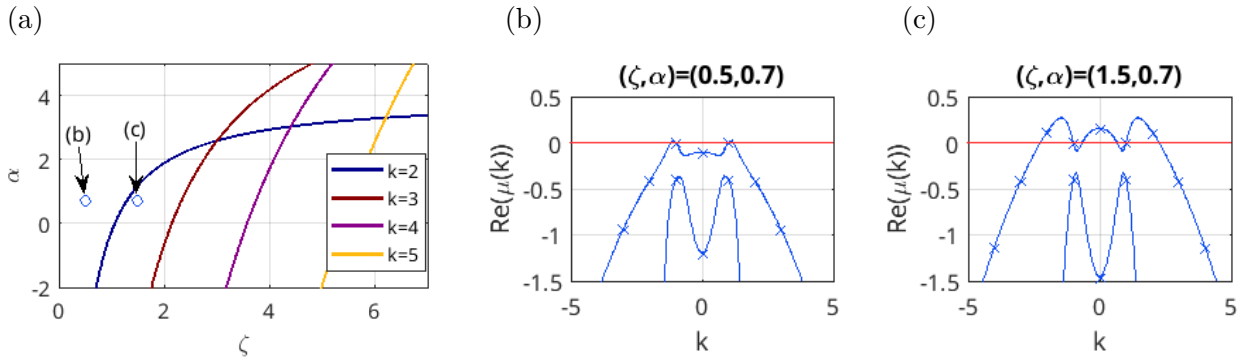

Figure 3: (a) Bifurcation curves obtained from (16) for $m = 2, 3, 4, 5$ in the ζ, α—plane for fixed $(\beta, \omega, D, \delta) = (1, 1, 0.1, 0.3)$. (b,c) Eigenvalues at points marked in (a).

for $\alpha > 4$ the $m = 2$ mode never becomes unstable.[5] Moreover, further analysis shows that no Hopf bifurcations can occur on $\mathbb{S}^1$ and hence to search for POs we must first follow the bifurcating steady state branches and "hope" for Hopf bifurcations on these. Essentially, these are also the reasons why we choose positive α: For small α ($\alpha < 0.5$, say) we find fewer Hopf points on the nontrivial branches, in particular no Hopf points on the $m = 2$ branch for $\alpha < 0$, and the rather large $\alpha = 3$ was chosen to put the $m = 3$ bifurcation before the $m = 2$ bifurcation.

2.2 Numerical continuation

We now use numerical continuation and bifurcation to compute the steady state branches $\mathcal{W}_m$ with wave number $m \geq 2$ bifurcating at $\zeta_c(m, \Lambda)$ from (16), and secondary bifurcations from these, including branches of POs arising from Hopf bifurcations. Throughout we fix

$$(\beta, D, \omega, \delta) = (1, 0.1, 1, 0.3) \tag{17}$$

and use ζ as the bifurcation parameter, for two cases $\alpha = 0.7$ and $\alpha = 3$. Additionally, for the sake of completeness, we first discuss the case $\beta = 0$. Here, the membrane decouples from ϕ and its dynamics are governed by the gradient Helfrich flow of the energy (4), with fixed $c_0 = \alpha$. For any given IC $X|_{t=0}$ with global flow, the ω–limit set then consists of a steady state shape X_∞ with associated Lagrange multiplier λ_∞. The bifurcation diagram thus consists only of steady states, and as ϕ follows κ we for simplicity drop the ϕ equation completely.

Subsequently switching on the coupling again, i.e., $\beta = 1$, we explore the more global behavior of the $\mathcal{W}_m$ branches, including their loss or gain of stability away from onset, and some secondary bifurcations of steady states, and of *relative* steady states, meaning rigidly drifting fixed shapes and ϕ coverages; these are computed as steady states with non–zero positional Lagrange multipliers τ_x and τ_y, see App.A.2.[6] As our main objective we then look at POs bifurcating at HPs from the (relative) steady state branches, and observe two major classes of interesting POs: breathers (breathing cells without net motion), and breathing *and* moving cells. In both, the length constraint restricts the amplitude of the POs, and the Lagrange multiplier λ for the length constraint must be treated as a dynamical variable, and similar we need Lagrange multipliers τ_x, τ_y and ρ for translation and rotation, respectively, thus yielding comoving frames with periodic speeds, again see App.A.2. We call the POs in these comoving frames *relative POs*, and plot these in the comoving frame, augmented by $t \mapsto (\tau_x, \tau_y, \rho)(t)$ if these are non–zero, and by the paths of the centers of mass of the cells in the labframe (e.g., Fig.6(c) and Fig.8(b–d)). Additionally, we use DNS to study the stability of POs.

[5] An analogous analysis is possible at the 2D sphere, and shows how to "tune" the bifurcation order from the sphere. However, this becomes considerably more complicated, as the Fourier modes e^{ims} must be replaced by spherical harmonics, cf. Rem. 1.1(a).

[6] In principle, there could also be rigidly rotating shapes, but such were not found, and instead we only find rotating relative POs, see below.

From this, besides the different ordering of m for the primary bifurcations, another difference between $\alpha = 0.7$ and $\alpha = 3$ is that for the former the POs found by Hopf bifurcation are all unstable, while for $\alpha = 3$ we find (meta)stable breathing $\mathcal{W}_4$ branches, bifurcating supercritically at a loss of stability of the steady $\mathcal{W}_4$ branch.

All numerics are based on `pde2path` [Uec21, pde26], in particular extending the `Xcont` setting [MU24b, MU26a] to PO computations, see App.B. Software sources for and further documentation of the computations can be found at [MU26b].

2.2.1 Intermezzo, $\beta = 0$: Destabilization via external pressure

The analysis in §2.1 shows that with ϕ "switched off", $\mathbb{S}^1$ is stable for all α. One way of destabilizing $\mathbb{S}^1$ in the purely mechanical model is by introducing an osmotic pressure P, which can also be seen as a Lagrange multiplier for an enclosed volume constraint (in 1D: enclosed area constraint). Hence for $\beta = 0$ we consider

$$\langle \gamma_t, \nu \rangle = \mathcal{G}_1(u) + P. \tag{18}$$

Without loss of generality we can set $c_0 = 0$, as c_0 only appears as c_0^2 in front of κ, and serves the same purpose as λ; then $\mathbb{S}^1$ is a steady state for any P, with $\lambda = \frac{1}{2} - P$.

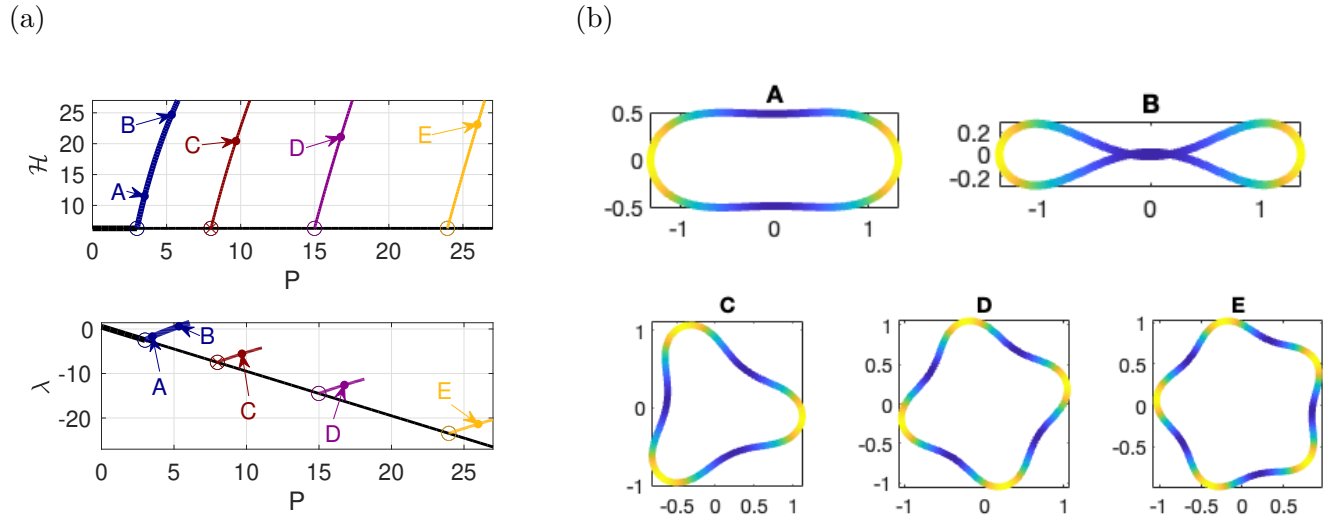

Figure 4: (a) Basic bifurcation diagram for (18), Helfrich energy $\mathcal{H}$ (top) and Lagrange multiplier λ (bottom) over the pressure P. Thick lines indicate linearly stable branches. (b) sample solutions.

Figure 4 shows a basic BD (BPs as ∘, stability/instability via thick/thin lines) and sample solutions. The black branch corresponds to $\mathbb{S}^1$ with $\lambda = \frac{1}{2} - P$ and constant area π. At $P = 3$ the circle destabilizes in a pitchfork bifurcation to the $\mathcal{W}_2$ wrinkling branch with decreasing area as P increases. The branch remains stable even beyond the point of self intersection, reached shortly before sample B. The further primary bifurcating branches $\mathcal{W}_3, \mathcal{W}_4, \ldots$ stay unstable throughout, and like $\mathcal{W}_2$ show self intersections at larger amplitudes. This is somewhat nonphysical, but clearly supported by the model. There are no secondary bifurcations on any $\mathcal{W}_k$ branches up to self intersection, quite in contrast to the 2D case [SBL90, MU24b], and also very different from the 1D case with morphogen, see below. Thus, by continuation and bifurcation we can only find $\mathbb{S}^1$ and $\mathcal{W}_2$ as stable branches, and this raises the question, if for any given P we can find other stable solutions via (length $L = 2\pi$ preserving) DNS. For this we perturbed a variety of (unstable) steady states from the $\mathcal{W}_3, \mathcal{W}_4, \ldots$ branches and used these as ICs for the Helfrich flow, and in all cases found convergence to the (possibly self intersecting) $\mathcal{W}_2$ solution at the given length. This shows that the 1D Helfrich model is rather restricted in its (length preserving) dynamics. We are now ready to look at the mechanochemical model.

2.2.2 $\alpha = 0.7$

For the coupled system (3) we use $(\beta, \omega, D, \delta) = (1, 1, 0.1, 0.3)$ and start with (fixed) $\alpha = 0.7$, and continuation parameter ζ. Figure 5 shows a basic BDs, and samples of steady states (see Remark 2.2 for BD plot conventions, and Fig.6 for samples of POs). From (16) we obtain that for increasing ζ the bifurcations from $\mathbb{S}^1$ occur in the order $m = 2$ (dark blue branch, samples A and B), $m = 3$ (red branch, sample C), $m = 4$ (violet branch, sample D), and $m = 5$ (lilac, no sample), and so on.[7] The average morphogen coverage

$$\langle\phi\rangle := \frac{1}{L_0}\int_\gamma \phi(s)\,\mathrm{d}s, \quad \text{resp.} \quad \langle\phi\rangle := \frac{1}{L_0 T}\int_0^T\int_\gamma \phi(s,t)\,\mathrm{d}s\,\mathrm{d}t \text{ for POs with period } T, \tag{19}$$

grows away from onset (a), while the surface tension Lagrange multiplier λ (resp. $\lambda = \langle\lambda\rangle = \frac{1}{T}\int_0^T \lambda(t)\,\mathrm{d}t$ for POs) decreases (b). In panel (c) we exemplarily show the translational Lagrange multiplier τ_y, becoming non–zero in the drift bifurcation of the light blue branch.[8]

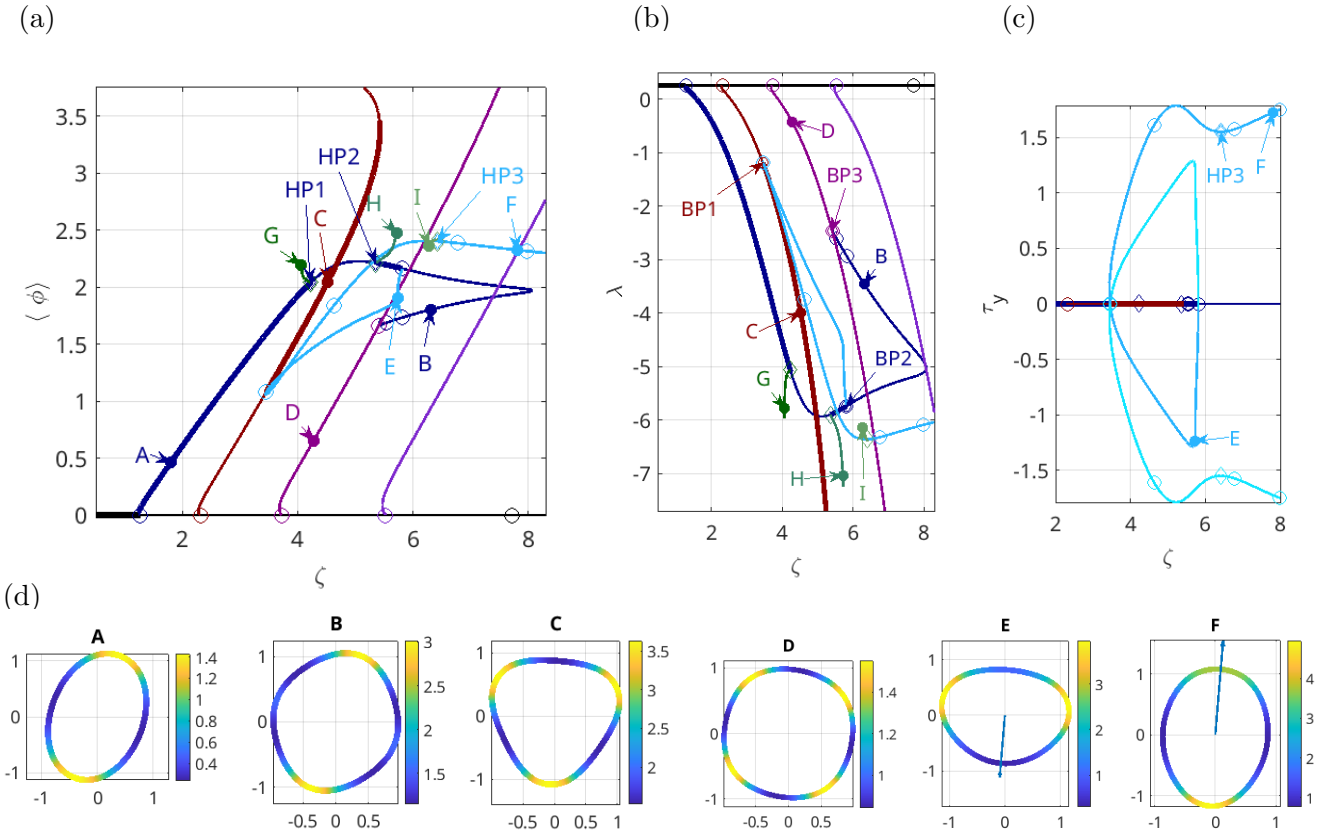

Figure 5: (a) Basic bifurcation diagram (BD) for (3) with parameters from (17) and $\alpha = 0.7$; $\langle\phi\rangle$ over ζ. (b) same branches with λ over ζ, where $\lambda = \langle\lambda\rangle$ for the (green) PO branches. (c) behavior of τ_y in and after the drift bifurcation(s) of the light blue branch. The very light blue branch in (c) corresponds to the "other directions", i.e., with the arrows in samples E and F flipped. (d) steady state samples; the arrows in E and F indicate the drift; see Fig.6 for PO samples.

Remark 2.2. In the BDs, thick/thin lines for steady state branches indicate linear stability/instability; for this, again the neutral translational and rotational modes are removed, as numerically they

[7] The primary bifurcations from $\mathbb{S}^1$ here are all subcritical for the given $\chi = 50$, with a fold shortly after bifurcation. Here we are mostly interested in the behavior of the nontrivial branches away from $\mathbb{S}^1$, but see §A.3 for further discussion of the local bifurcations from $\mathbb{S}^1$ and their amplitude equations, and how that depends on χ.

[8] The drift–in–x multiplier τ_x is also nonzero on the light blue branch; no rotation is picked up in any of the (relative) steady states, i.e., $\rho = 0$, but this will change on (some of) the PO branches, see Fig.6.

yield eigenvalues of order 10^{-6} with uncontrolled positive or negative real parts. For PO branches, no stability information is included in the BDs, and stability is discussed subsequently via DNS. BPs are indicated by $\circ$, HPs by $\diamond$, and sample points by $\bullet$, and labeled A, B, ..., respectively PO1, PO2,.... The labeling of the BPs (no labels given to BPs in Fig.2) and HPs is Figure–wise, not branch-wise, i.e., HP3 in Fig.5 is the third HP in the figure, but the first on the light blue branch. ⌋

The $m = 2$ branch is stable up to HP1 at $\zeta \approx 4.2234$ where the PO branch with sample G bifurcates. It is also again stable between HP2 at $\zeta \approx 5.3593$ (PO branch with H) and the BP at $\zeta \approx 5.8172$ (labeled BP2 in (b)), where the branch with sample E bifurcates, which connects to the $m = 3$ branch at a BP at $\zeta \approx 3.4547$ (labeled BP1 in (b)), after which it continues to sample F and higher ζ. Notably, the bifurcations at BP1 and BP2 are *drift bifurcations*, meaning that here the vesicles pick up a drift speed, indicated by the arrows in E and F, and by the translational Lagrange multiplier τ_y over ζ BD in (c). Naturally, BP1, where the $\mathcal{W}_3$ branch and light blue branch meet, is a double BP: the kernel is spanned by vectors yielding the moving out or in of exactly one of the corners, yielding acute or obtuse triangles (like E), while distortion of the third corner corresponds to a linear combination of the two kernel vectors describing the other corners.[9] Note that the bifurcations at BP1 are transcritical, and at BP2 pitchforks, which again follows from symmetry. Finally, the $m = 2$ branch itself connects to $m = 4$ at $\zeta = 5.4111$ (labeled BP3 in (b)), in a period (in s) halving pitchfork.

The $m = 3$ branch is stable between BP1 and the fold at $\zeta \approx 5.4304$. After this fold, it continues to larger $\langle\phi\rangle$, and for instance then features a HP at $\zeta \approx 4.049$ (not shown). For later comparison, here we remark that using DNS to test the linear stability indicated by the thick lines in Fig.5 generally yields the following: for small perturbations of ϕ or X from a stable steady state not close to a BP, FP or HP, we typically obtain convergence back to the perturbed steady state, but for larger perturbations the flow often goes to some "run and tumble" dynamics, discussed below in detail for $\alpha = 3$. Here we summarize that already concerning just (relative) steady states the BD for (3) already becomes rather complicated, with many secondary bifurcations from and interconnections of the primary branches.

Fig.6 shows the three PO samples indicated in Fig.5 as G,H,I. The top pictures show the shapes along the POs, with $\gamma(s,t)$ colored by $\phi(s,t)$, where s is the arclength along $\gamma(\cdot,t)$; the red lines indicate the $s = 0$ coordinate lines for the bottom $\kappa(s,t)$ plots. The middle panels show the behavior of λ and $\langle\phi\rangle$ over t, indicating that both G and H are of relaxation oscillation type. The Lagrange multipliers τ_x, τ_y and ρ for the rotational and translational constraints are zero ($< 10^{-6}$ in modulus) for these POs, i.e., G and H are genuine breathers without hidden rotations or translations. The plots of $\kappa(s,t)$ at the bottom show how κ behaves along the POs; below we shall use such κ plots to illustrate more complicated dynamics. For I, we additionally show (τ_x, τ_y, ρ). Because the branch with I bifurcates from a branch of uniformly drifting relative steady states, we already know that the averages $\langle\tau_x\rangle$ and $\langle\tau_y\rangle$ must be non–zero at bifurcation, and additionally the PO I picks up a time periodic non-zero rotational Lagrange multiplier ρ, but with $\langle\rho\rangle \approx 10^{-6}$. Thus, we obtain a net translation of γ over one period, but no net rotation; the last plot in (c) shows the space–time path of the center of mass (COM) of the moving vesicle, and its projection (red) into the x–y–plane.

All POs in Fig.6 must be unstable. While the branches with G and H bifurcate at a stability loss/gain, and hence could yield stable PO branches, these POs bifurcate subcritically in both cases. Now, running DNS (see App.B.1 for details) from small perturbations of any time slice $(X,\phi)_{t=t_0}$ of POs G or H, usually taking $t_0 = 0$, we get convergence back to the $\mathcal{W}_2$ branch at the respective ζ value. The PO branch with I bifurcates from an already unstable steady state, and at this ζ range we do not find *any* stable steady states. Thus, we cannot expect convergence of perturbations of I to

[9] In the software, we just find a two dimensional kernel of this D_3 symmetry breaking bifurcation, and predictors for the three bifurcating branches must be found by (numerically) solving the so called algebraic bifurcation equations; see also [Uec21, §2.5.3] for a simple example of equivariant bifurcations with D_3 symmetry.

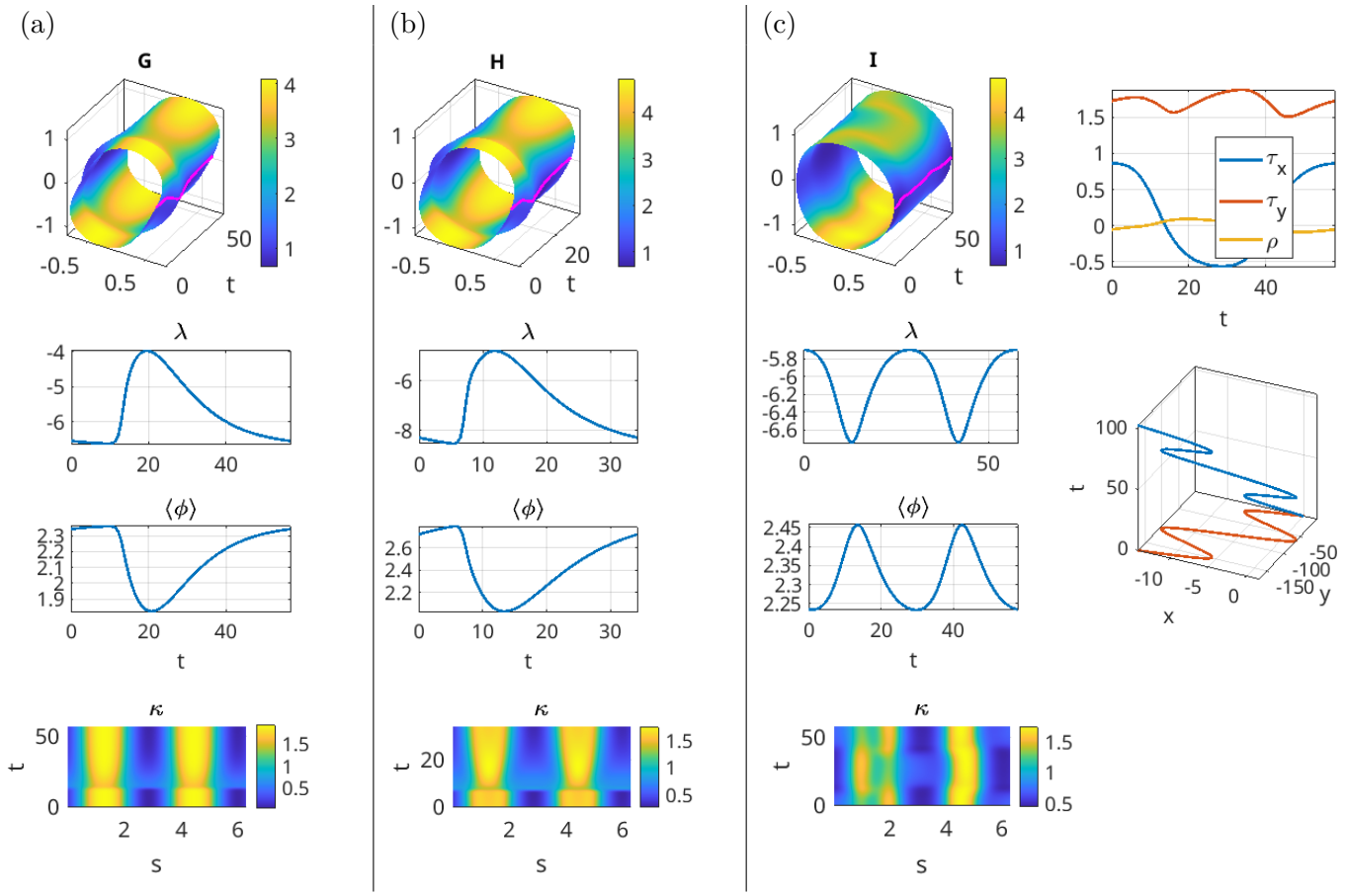

Figure 6: PO samples G (a), H (b) and I (c) from BD in Fig.5. Top to bottom: shape of γ along PO, with $\phi(\cdot, t)$ plotted on γ; λ and ϕ over time t, for G and H showing the relaxation nature of the POs; and κ. For I we also plot the dynamic moving frame multipliers τ_x, τ_y, and ρ (top right), and the space–time path of the center of mass of the cell (middle right). For G,H, τ_x, τ_y, and ρ are zero ($< 10^{-6}$ in modulus).

some steady state, and indeed such DNS yield self-intersection (and subsequent failure of the DNS) after rather short times.

In summary, for $\alpha = 0.7$, and altogether in the range $\alpha \in (0, 1.5)$, say, and forcefully for $\alpha \leq 0$, the model (3) only seems globally well-posed in general for small ζ ($\zeta < 5$ for $\alpha = 0.7$), where the dynamics is dominated by stable steady states with small m. Some of the steady state branches with small m extend to larger ζ, and higher m branches bifurcate and exist at arbitrary large ζ, but these are all unstable, and general ICs lead to self intersections and (numerical, and likely also analytical) blow–up. Moreover, we could not find any stable POs. However, both of these points change at larger α, as shown in the next section.

2.2.3 $\alpha = 3$

We now turn to the second regime, $\alpha = 3$, for two reasons: (i) in this case, the order of primary bifurcations is $\zeta_3 \approx 3.199 < \zeta_2 \approx 4.201 < \zeta_4 \approx 4.2829$, i.e., we have "tuned" the primary bifurcations to the $\mathcal{W}_3$ branch bifurcating first. (ii) this naturally has further consequences for the secondary bifurcations, and inter alia we now find stable $\mathbb{Z}_2 \times \mathbb{Z}_2$ symmetric breathers bifurcating from the $\mathcal{W}_4$ branch.

Figure 7 shows a basic BD of the three primary branches $\mathcal{W}_3$ (brown, with sample A), $\mathcal{W}_2$ (blue, with sample D_1, see also the zoom inset at the bottom right), and $\mathcal{W}_4$ (violet, with sample B, also already previewed in Fig.2(a)), two secondary steady state branches (with samples C and D_2), and five PO branches (green, orange, and black, with labels E–I, see also zoom inset at the top left). We start with the $\mathcal{W}_2$ branch, which here bifurcates more strongly subcritical and on the other hand after two folds reconnects with the $\mathcal{W}_4$ branch, see zoom inset. The $\mathcal{W}_2$ branch is hence not of major

interest to us, and just illustrates the strong effect the coupling with ϕ can have also close to $\mathbb{S}^1$. For completeness, we also note that there is a second $\mathcal{W}_2$ branch bifurcating from $\mathcal{W}_4$ at large amplitude, with sample D_2, which however is unstable throughout.

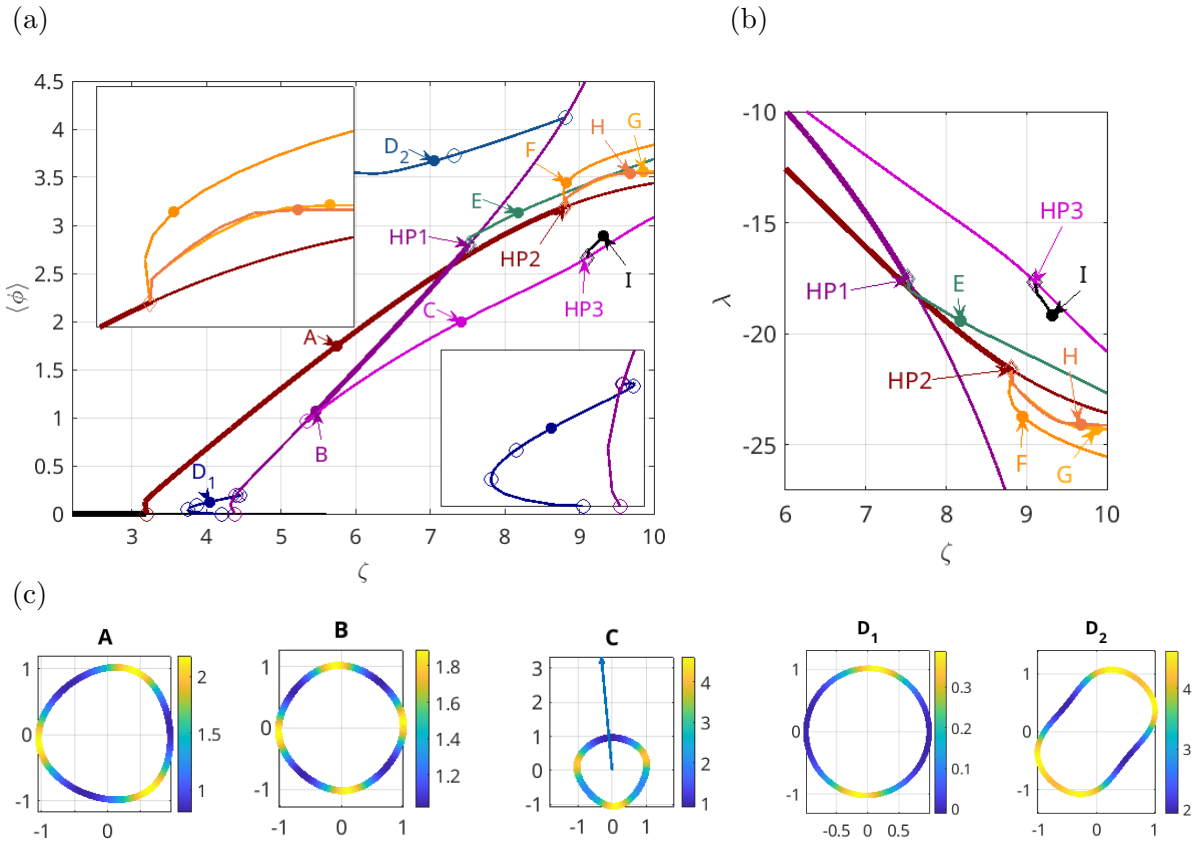

Figure 7: Basic BD for (3) with parameters from (17) and $\alpha = 3$, and steady state samples (C a relative steady state, as indicated by the arrow of rigid translation); see Fig.8 for PO samples.

The $\mathcal{W}_4$ branch becomes stable in a double BP at $\zeta \approx 5.3439$. Here the kernel is spanned by vectors describing the moving out and in of two opposite "corners", which can occur in two orientations. The magenta branch with sample C is one (direction of one) of the bifurcating branches, namely with the top corner moving in (and the bottom slightly moving out), such that the D_4 symmetry is broken to $\mathbb{Z}_2$. As a result, this is again a drift bifurcation, with the picked up speed indicated by the arrow in sample C. On this branch there is a Hopf point, and the POs bifurcating there also pick up some rotation, similar to sample H discussed below.

The $\mathcal{W}_4$ branch then loses stability again at $\zeta \approx 7.5216$ in a *simple* HP labeled HP1. From symmetry it then follows that a single branch of POs must bifurcate, on which solutions alternate between two $\mathbb{Z}_2$ symmetric shapes, i.e., a breather, without drift or rotation, see sample E (already previewed in Fig.2(b)). As this Hopf bifurcation is supercritical, we expect these breathers to be stable, at least near onset, although this stability is difficult to analyze due to the always present zero modes from spatial translations and rotations. Numerically, we find the bifurcating solutions to be *metastable* under DNS in the labframe, i.e., only stable over long transients, but stable under constrained DNS, see Fig.9, and the discussion there.

The situation is more difficult at the *double HP* on $\mathcal{W}_3$ labeled HP2 at $\zeta \approx 8.815$, where $\mathcal{W}_3$ loses stability. The Hopf eigenspace here is spanned by two vectors each describing the dominant motion of just one corner, and by symmetry a dominant motion of the third corner can be described by a linear combination of the first two. From D_3 symmetry it follows that at least (and generically exactly) three PO branches must bifurcate, modulo conjugacy, see Remark 2.3.

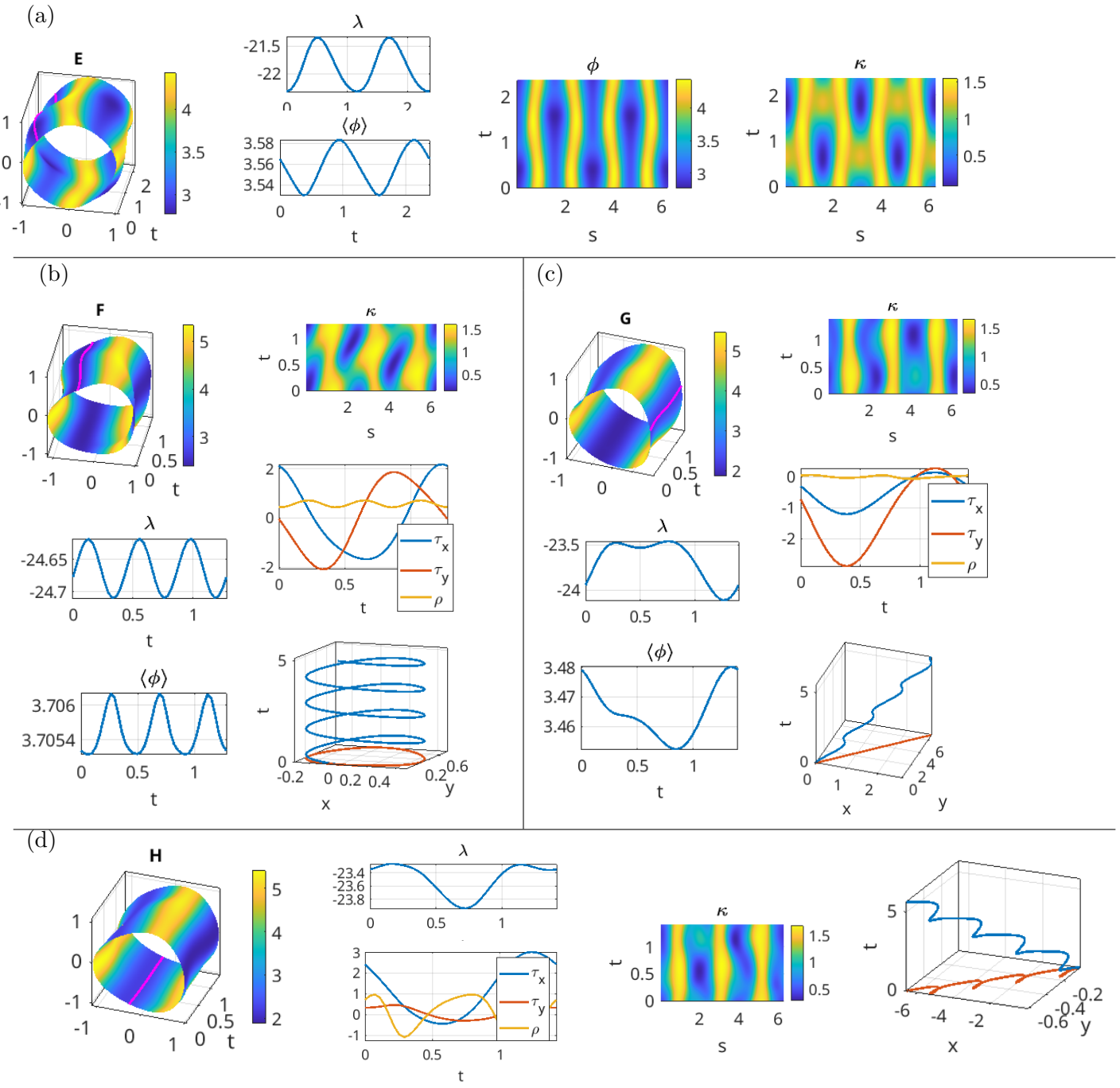

Figure 8: PO samples for Fig.7; (a) $\mathbb{Z}_2 \times \mathbb{Z}_2$ symmetric breather; (b-d) (relative) TW and SWs bifurcating from the D_3 symmetric HP2. See text for details.

Figure 8 illustrates four PO samples marked E–H in Fig.7. As already said, E in (a) is a "breather", and in particular the translational and rotational Lagrange multipliers τ_x, τ and ρ are $< 10^{-6}$ (in modulus) and hence not shown. The two $\mathbb{Z}_2$ symmetries (along $s = 0$ and $s = \pi$), together with the $(s, t) \mapsto (s + \pi/4, t + T/2)$ symmetry can clearly be seen. For PO F in (b), $\tau_x, \tau, \rho \neq 0$, but still $\langle \tau_x \rangle = 0$ and $\langle \tau_y \rangle = 0$, and hence there is no net motion over one period T; the space–time plot of the COM in the last plot in (b) forms a helix, and the projection in the x–y plane a closed loop. We believe that the best name for this kind of PO is "modulated traveling wave", see also the κ plot in (b). In contrast, for PO G in (c) we see a "stick–slip" motion of the cell in the lab frame. Here, the top "corner" at $s = s_0 \approx 1$ oscillates most strongly, and the two other corners follow with equal phase, and hence γ alternates between an obtuse and an acute triangle. Letting $\vec{v} = (\cos(s_0), \sin(s_0)) \approx (1, 2)/\sqrt{5}$ this yields motion in direction $\vec{v}$, sticking (in fact slightly reversing) when γ is obtuse, and slipping when γ is acute. See the COM mass plot, with projection in the x–y

plane a line in direction $\vec{v}$. In (d), the third PO H bifurcating from the triple HP HP2 can be seen as a superposition of F and G. Moreover, we note that the PO I bifurcating from the branch of rigidly translating vesicles (see sample C) is very similar to the PO H.

Remark 2.3. The three branches with samples F,G and H bifurcating at HP2 in Fig.7 and illustrated in Fig.8(b–d) represent the three conjugacy classes (equivalency of POs under rotation by $2\pi/3$) of branches bifurcating at double HPs in the D_3 symmetric case, in the one-dimensional fixed point subspaces of the D_3 group action. In the numerics, to search for different branches of POs bifurcating at HPs of higher multiplicity $n \geq 2$, we optionally pass a vector $(z_1, \ldots, z_n)$ of coefficients for the different eigenvectors $\Psi_1, \ldots, \Psi_n$ to the pertinent frequency ω_H to the branch switching routine[10], which then creates the predictor

$$U_{\text{pred}}(s, t; z) = U_H(s) + \mathrm{d}\sigma[(z_1\Psi_1(s) + \ldots + z_n\Psi_n(s))\mathrm{e}^{\mathrm{i}\omega_H t} + \text{c.c.}], \tag{20}$$

for branch switching to a PO branch. In the double D_3 HP cases, different choices of z_1, z_2 then always takes us to one of the branches with F,G or H, modulo conjugacy, i.e., modulo rotation of γ (and hence the COM paths) by $2\pi/3$, or, in rare cases, non–convergence of the corrector for the PO computation. This agrees with the general theory for D_3 equivariant Hopf bifurcations, see for instance [DP06] and the references therein, which yields that there generically bifurcate exactly three (not just at least three) branches (modulo conjugacy) of POs at double HPs. ⌋

2.2.4 Stability and DNS

In Fig.9(a-d) we present DNS *in the lab frame*, i.e., using (45), with a perturbation of the $t = 0$ time slice of PO E as IC. The PO E in principle should be stable as the branch bifurcates supercritically at the stability loss of the $\mathcal{W}_4$ branch (again after removing the neutral modes, see Remark 2.2). However, in our straightforward (unconstrained) DNS, the solutions only appear to be metastable, i.e., stable on long but finite timescales (up $t = t_0 = 14$, say). We believe this is due to (unavoidable) numerical errors interacting with the neutral translational and rotational modes. Once these get sufficiently strongly excited (after $t = t_0$), a net motion sets in (see the COM path in (d), and the axis ticks in (a)), and in its comoving frame the solution goes to a roughly periodic (but with decreasing amplitude, see (b) after $t = 25$) source–sink pair dynamics for κ (and ϕ) on γ, somewhat similar to the trigger waves from Fig.1. For smaller amplitude initial perturbations, and/or for POs closer to HP1, i.e., for smaller amplitude non–moving breathers, we obtain longer metastability, but eventually we always end up with source–sink pairs, in which moreover $\lambda(t)$ ($\langle\phi(t)\rangle$) always goes to a higher (lower) level.

In the constrained DNS (cDNS, cf. (46)) in Fig.9(e), trading spatial translations for translational Lagrange multipliers, the PO E becomes genuinely stable. This shows some inconsistency between (45) and (46), which however only appears after many periods of oscillations (also depending on the initial perturbation), and as already said we believe that over long times the unconstrained DNS in (a-d) might be less reliable than the cDNS in (e) due to uncontrolled neutral translational (and rotational) modes in (a-d).[11]

[10] see also [Uec21, §7.2.3] for an example of double HPs in an example with D_4 symmetry

[11] In cDNS, here we only use the translational multipliers τ_x and τ_y, and no constraint for rotations; however, these do not get excited, and we obtain the same results for cDNS including such rotational constraints. Moreover, we checked that the cDNS here and all other cases gives the same results when using a simple implicit Euler scheme (which can be overdamping) for the DAEs, and when using the high order DAE–suitable code `RADAU`, see the discussion after (46). On the other hand, `RADAU` typically only works for a few steps in DNS (without translational and rotational constraints), and then yields excessive step–size reductions and eventually non–convergence. Therefore, the presented (lab frame) DNS are always done with implicit Euler.

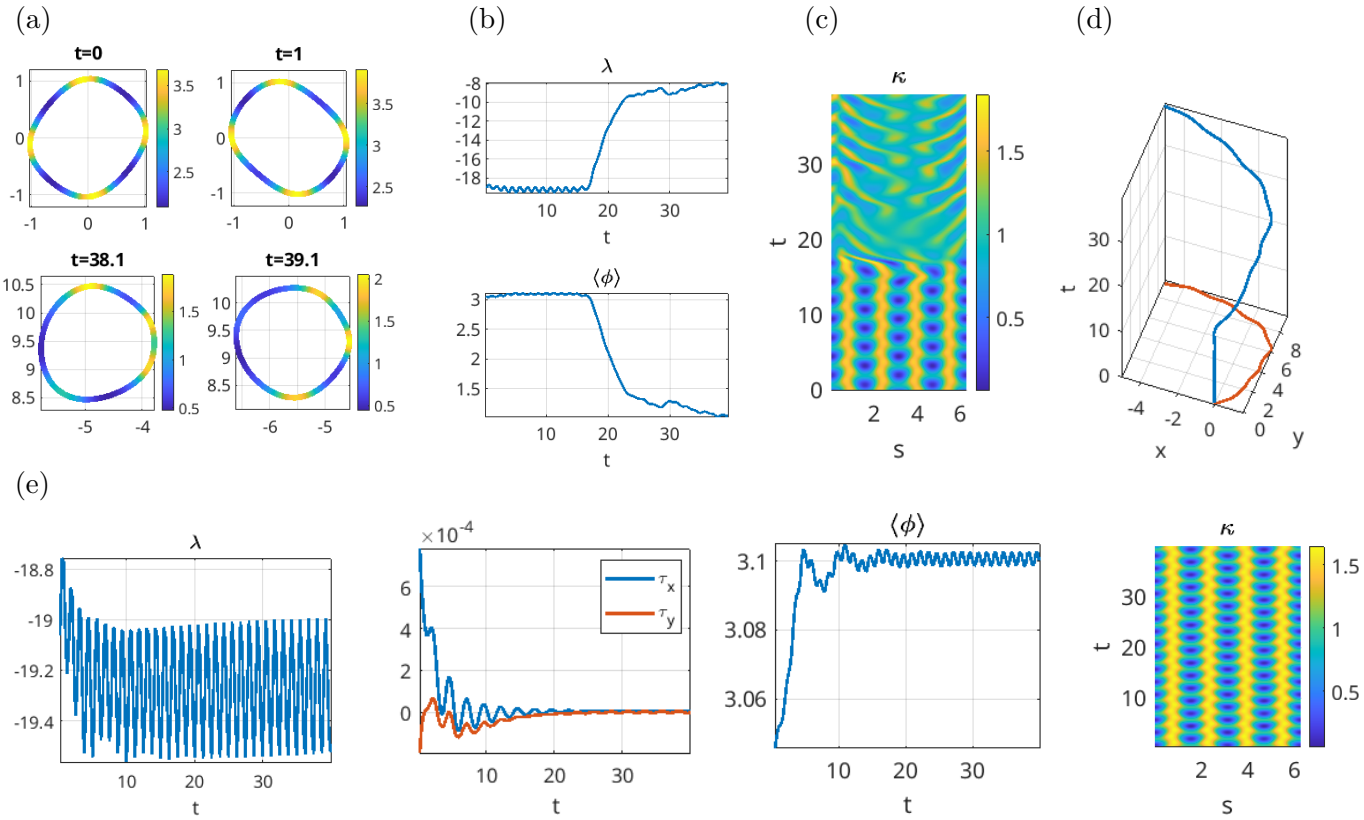

Figure 9: (a) Snapshots from DNS from perturbations of the PO E time $t = 0$ slice, $X|_{t=0} = X_0 + a\cos(3\vartheta)N$ with amplitude $a = 0.01$. (b) time–series of λ and $\langle\phi\rangle$. (c) (together with (a)) illustrates the convergence to a tumbling vesicle with a source–sink pair (trigger wave) for κ. (d) shows the COM path of the vesicle. (e) cDNS with `imEuler`, but same with `Radau` (in (a-d) up to $t = 20$, then failure).

For initial perturbations of the $t = 0$ slice of the D_3 symmetric POs F,G, and H we obtain the following, see Fig.10. Under DNS (a), F is unstable and after a rather short transient yields trigger waves. On the other hand, for cDNS, F shows some metastability: starting from a moderate initial perturbation (of amplitude 0.1 times the amplitude of the PO F), the solution shows periodic behavior up to $t \approx 20$, which is best seen in the behavior of τ_x and τ_y, and the s–t plot of κ. Subsequently, the shapes of the oscillations deteriorate, and at $t \approx 23.2$ `RADAU` fails, while implicit Euler leads to self–intersection and subsequent failure. Finally, DNS from G,H are genuinely unstable in both, DNS and cDNS. In DNS, they again yield convergence to trigger waves, and in cDNS self intersection (c, for G), and similar for H.

3 Experiments in 2D

Having obtained some understanding of the multitude of possible steady states, POs, and dynamics, for (3) in 1D in §2, we come back to the 2D problem (2), with one sample PO already given in Fig.2(c). The analytical and/or numerical classification and stability problem of possible steady states and POs in 2D in dependence of parameters becomes *much* harder, mostly due to the higher multiplicity of BPs and HPs in 2D, also related to the larger symmetry group $O(3)$ of rigid body motions of the sphere compared to $O(2)$ for the circle. Thus, here we mainly restrict to one basic BD to which the PO from Fig.2(c) belongs, and give some DNS experiments.

Panel (a) in Fig.11 shows selected steady state branches for $\alpha = 2$, and two PO branches. Steady state samples are given in (b); (c) shows a PO sample from the first PO branch with tetrahedral symmetry, already previewed in Fig.2, and (d) shows a sample from PO2 with hexahedral symmetry. The bifurcations from the sphere happen in spherical harmonic order l=3 at $\zeta\approx$3.2945 (BP1), l=4

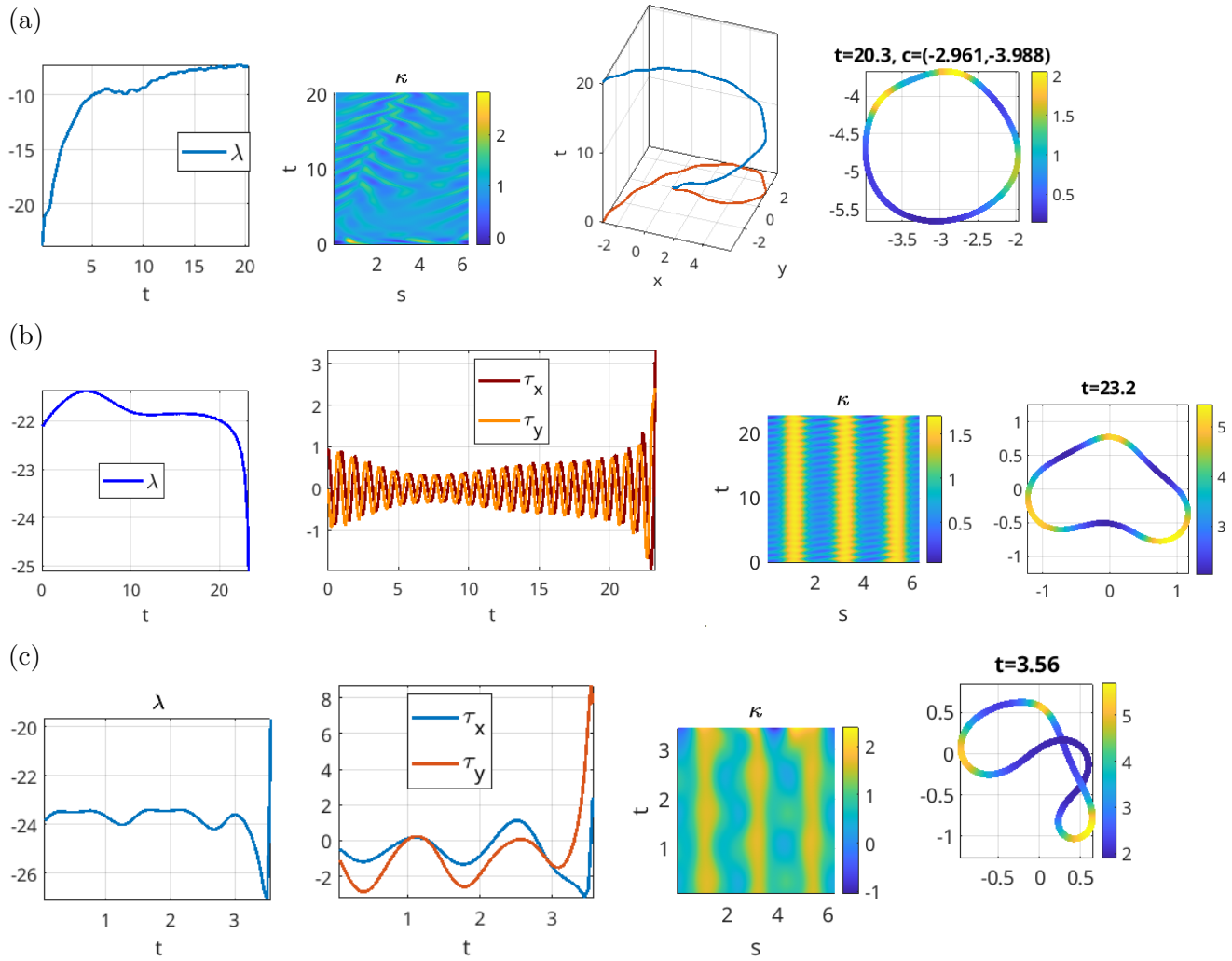

Figure 10: (a) DNS from F emergence of traveling vesicle with trigger waves. (b) cDNS from F, metastable behavior, but eventual self–intersection in implicit Euler, and failure of RADAU. (c) cDNS from G, unstable, self intersection (and failure of RADAU) at small t.

at $\zeta \approx 4.5732$ (BP2) and l=5 at $\zeta \approx 6.3433$ (not shown). For l=3 at BP1, the kernel is hence 7-dimensional, and for l=4 at BP2 it is 9-dimensional, and at BP1 we only compute two bifurcating steady state branches, and three at BP2. We start the discussion with the brown regular tetrahedron branch with HP1. This branch becomes stable at the Hopf bifurcation of breathing tetrahedra, and loses stability in a steady state bifurcation at $\zeta \approx 4.97$ to "distorted" tetrahedra (not shown). The branch with A, with solutions with 5 unequal spots bifurcates simultaneously with the tetrahedral branch at BP1, together with several other branches. Similarly, we show three steady state branches bifurcating at BP2, of which the green one is most interesting as it gains stability at HP2, where the PO2 branch of breathing hexahedra bifurcates. Both, HP1 and HP2 are simple, and in summary, the bifurcating PO branches of breathing tetrahedra and hexahedra are analogous to the breathing D_4 branch with sample E from Fig.8(a). In particular, the three translational and the two rotational Lagrange multipliers are all zero on the branches with PO1 and PO2.

As in 1D, the (linearized, i.e., spectral) stability of steady states is indicated by thicker lines, and we checked that this fully agrees with stability obtained from DNS starting with small perturbations of linearly stable steady states. For the POs, we may expect stability of PO1 as the branch bifurcates supercritically from the tetrahedral branch, while PO2 must be unstable as its branch bifurcates subcritically. To assess dynamics near these POs, and more general dynamics also yielding further stable steady states at larger ζ, we again resort to DNS, similarly as in 1D as DNS in the lab frame, and as cDNS, now with additional translational Lagrange multipliers (τ_x, τ_y, τ_z).[12]

[12]Again, the rotational neutral modes appear to be less dangerous here, and hence we do not add constraints and

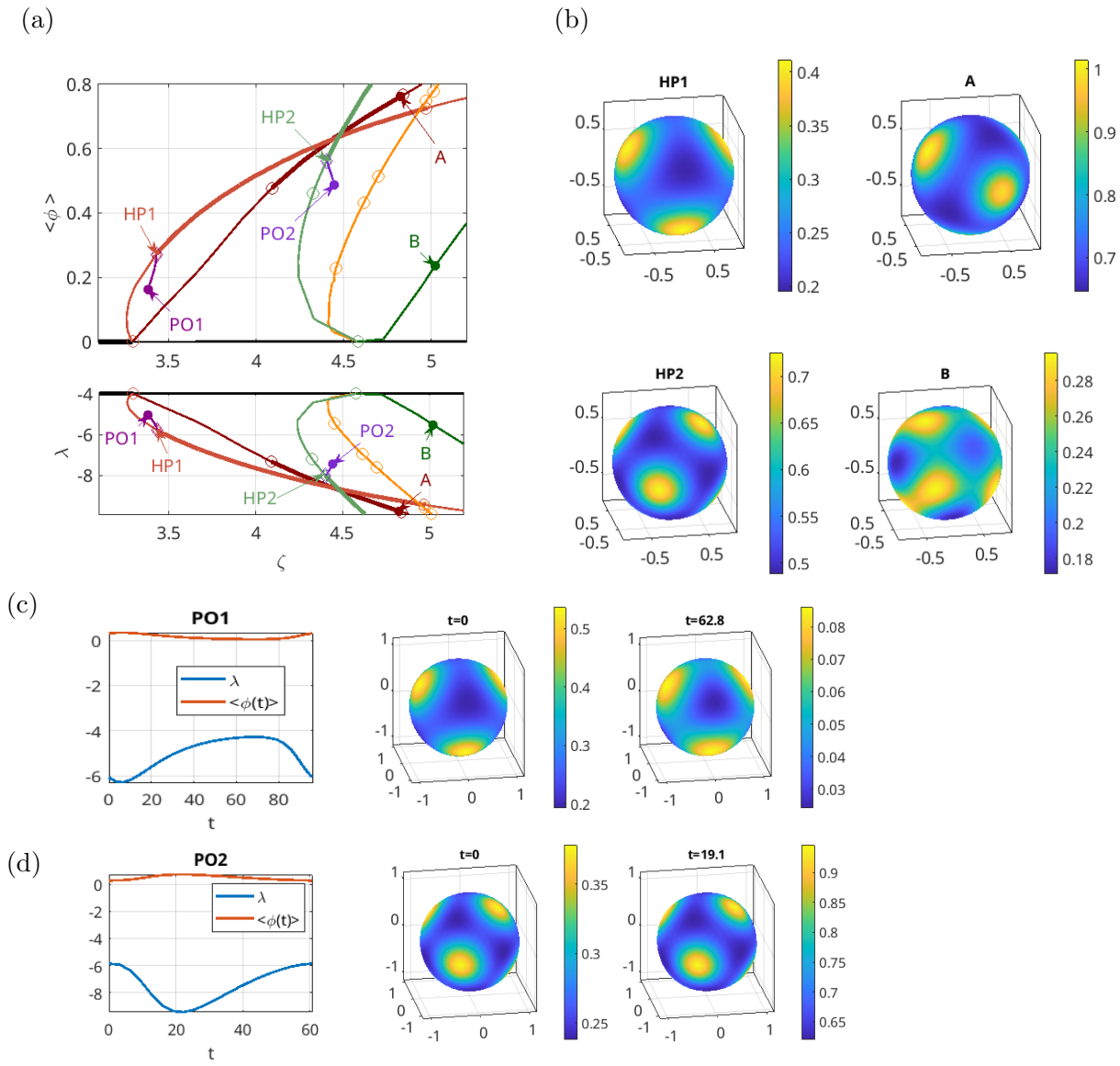

Figure 11: BDs (a) and steady state samples (b) for (2) with $(\beta, \omega, D, \delta)$=$(1, 1, 0.1, 0.05)$ and $\alpha = 2$. First bifurcation from the sphere at $\zeta \approx 3.29$ to l=3 spherical harmonics (7 dimensional kernel), and second bifurcation at $\zeta \approx 4.57$ to l=4 (9 dimensional kernel). At both BPs we only show selected bifurcating branches. (c,d) PO1 and PO2 samples.

In Fig.12 we contrast the labframe DNS in (a) with cDNS in (b). The time series for λ and $\langle\phi\rangle$ in (a) show some similarity (in period and amplitude) to those of PO1, but like in 1D we also get some irregular tumbling and motion of the vesicle (COM path in 2nd plot), together with shape deformations which lead to the appearance, shifting and merging (e.g., near $t = 500$) of the spots of ϕ in the snapshots on the right. However, except during these transitions we mostly observe 4 spots in ϕ, and roughly tetrahedral symmetry. In contrast, in (b) we take a rather large perturbation of the $t = 0$ time slice from PO1, and get convergence back to PO1, with the translational Lagrange multipliers (τ_x, τ_y, τ_z) staying small for very long times (up to $t = 2000$).

Finally, in Fig.13 we use cDNS at larger ζ, and obtain convergence to stable steady states (of higher spherical harmonics type), and this seems to be the generic behavior for the given parameters, up to $\zeta = 12$. However, the associated steady state branches are rather difficult to continue at larger ζ, due to loss of symmetry during the continuation, indicating branch jumping. See, e.g., [ZHL17] for numerical methods to enforce a given symmetry on a solution branch in the related problem of

Lagrange multipliers for these in cDNS.

two–phase vesicles.

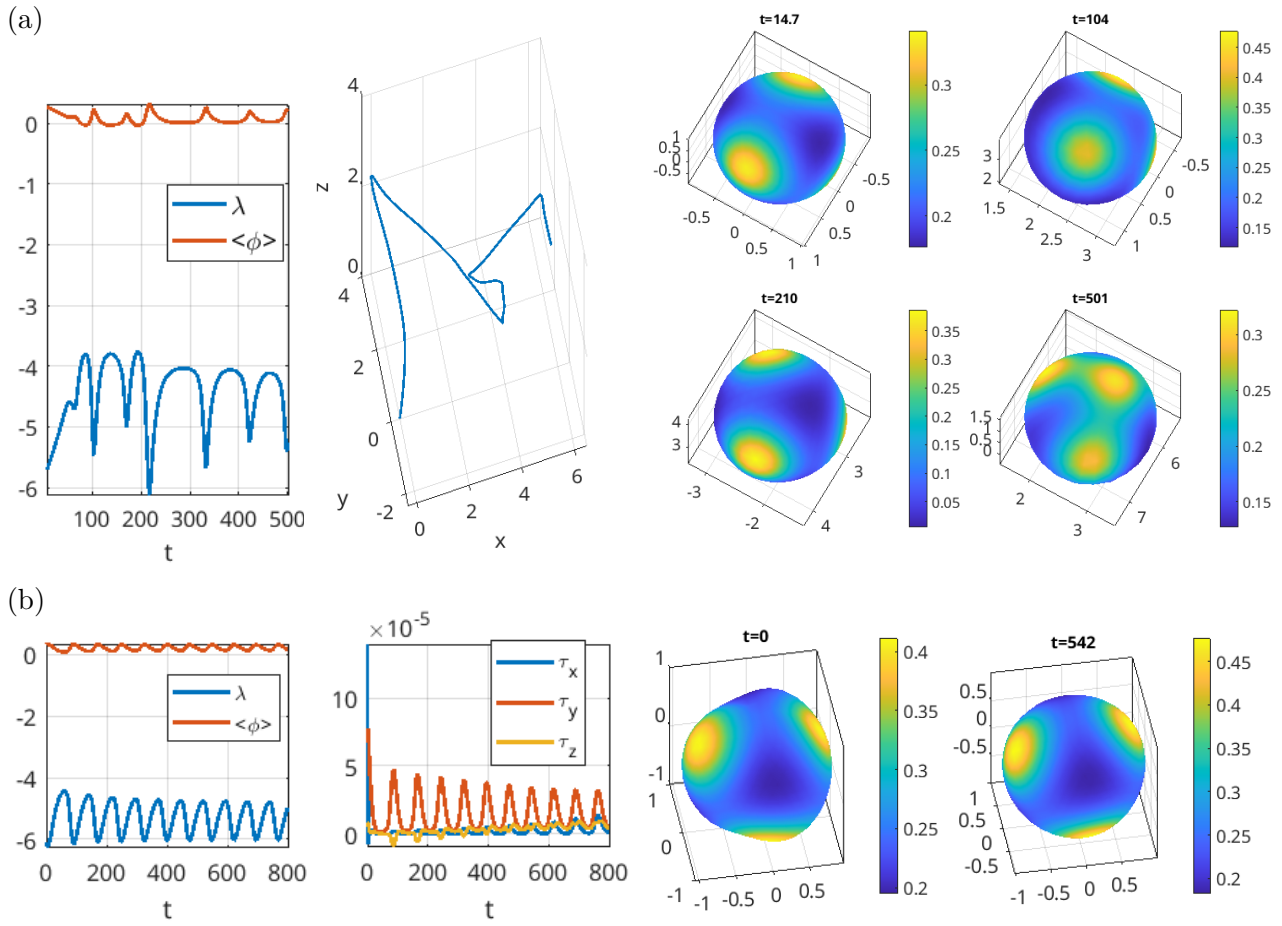

Figure 12: (a) DNS starting near HP1 from Fig.11; drifing and tumbling vesicle, with numbers of ϕ spots alternating between 4 and 5. 2nd plot is the COM path. (b) cDNS starting from a (rather large) perturbation of the $t = 0$ slice of PO1, showing stability of PO1 under cDNS.

4 Discussion and outlook

We studied what we believe to be one of the simplest geometric mechanochemichal models, which couples the Helfrich gradient flow for the vesicle membrane X (resp.γ in 1D) with a reaction–diffusion equation for a single morphogen ϕ on X (resp. on γ), via the dependence of the spontaneous curvature as $c_0 = \alpha + \beta\phi$, and conversely via the kinetics $\zeta \dfrac{f(\kappa)}{\omega + f(\kappa)}$ for ϕ. We focused on the 1D case, which is already very rich in steady and dynamical pattern formation, and for 2D restricted to an outlook.

Our primary continuation parameter was ζ, and guided by the linear stability analysis at the circle in §2.1 we took two different values for α with remaining parameters fixed: For small $\alpha = 0.7$ (§2.2.2), the primary loss of stability of $\mathbb{S}^1$ is wrt to spatial wave number $m = 2$ steady patterns, then $m = 3, m = 4, \ldots$. However, larger α can be used to sort larger m to the front, and in §2.2.3 we used $\alpha = 3$ yielding the order $m = 3, 2, 4, \ldots$. In both cases, we find HPs on the primary bifurcating branches, some of these of higher multiplicities, and from these HPs bifurcations of POs, which essentially come in two variants: *breathing* vesicles, i.e., POs G,H from Fig.6, and PO E from Fig.8, and *breathing and moving* vesicles, i.e., PO I from Fig.6, and POs F,G,H from Fig.8. Additionally, there are bifurcation from steady states to relative equilibria with non–zero translational Lagrange multipliers τ_x, τ_y, which corresponds to uniformly translating vesicles, see samples E,F in Fig.5 and C

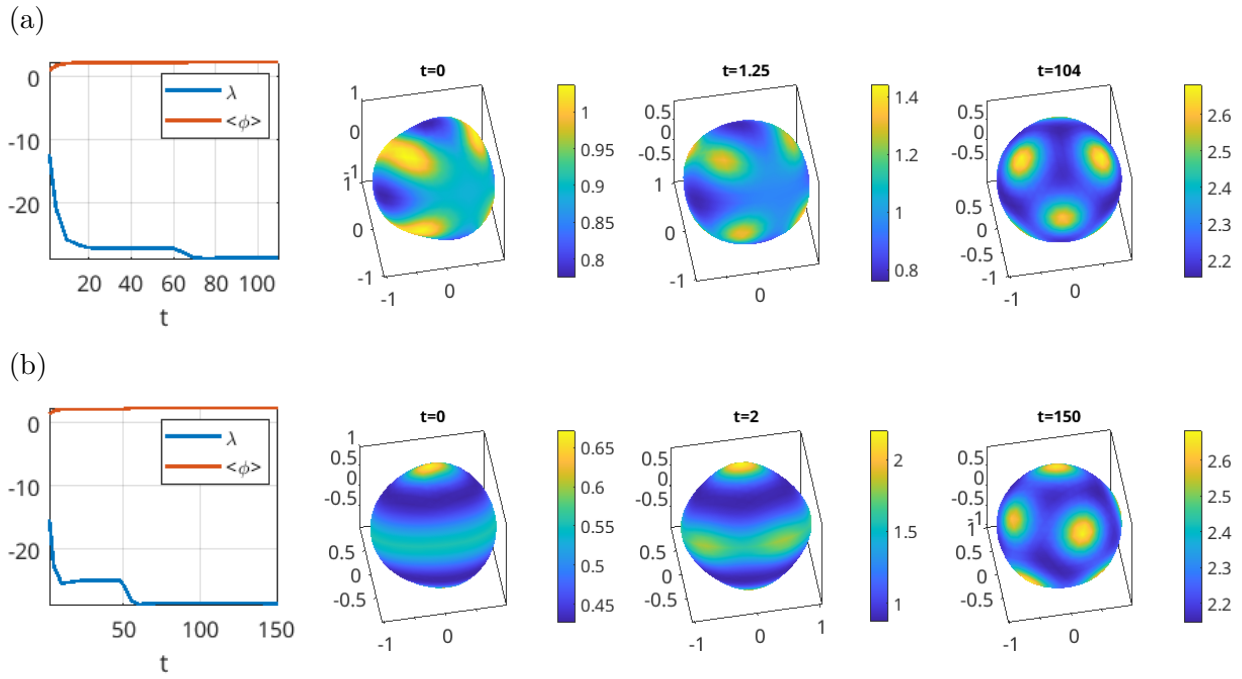

Figure 13: (a) cDNS from perturbation of B from Fig.11 but at $\zeta = 8$; convergence to stable octahedron. (b) cDNS from pertubation of solution on orange branch at $\zeta \approx 4.7$ (see $t = 0$ plot in (b)), but at $\zeta = 8$; convergence to stable 9–hedron. In both cases τ_x, τ_y, τ_z converge to $O(10^{-4})$ constants.

in Fig.7. Naturally, HPs on such branches also yield breathing and moving vesicles, which moreover pick up some rotation.

Next we used DNS to assess the stability of POs and more general dynamics. We distinguish between "labframe" DNS, or just DNS, and constrained DNS (cDNS), which expresses translations again via the multipliers τ_x and τ_y.[13] These two versions of DNS initially behave identical, but may deviate at large t: We believe that in (unconstrained) DNS numerical errors accumulate to excite the neutral (translational and/or rotational) modes, and as result for instance the D_4 symmetric breather PO E from Fig.8 is only metastable in DNS, but fully stable in cDNS, cf. Fig.9. Similarly, we believe that the D_3 symmetric (moving and rotating) breather F from Fig.8 should be dynamically stable, but very quickly yields trigger waves under DNS, and also under cDNS is only metastable, leading to numerical failure after about 20 periods. On the other hand, DNS when not converging back to (stable) steady states generically goes to tumbling vesicles with periodic behavior of ϕ on γ, i.e., source–sink pairs as in Fig.9(a–d), Fig.10(a).

We found analogous steady state bifurcations in 2D, and then focused on breathing vesicles, namely the two POs PO1 and PO2 from Fig.11. The general dynamics in 2D seem similar to 1D, but generally more complicated. In our experiments for $\alpha = 2$ in §3, when not starting near stable steady states, DNS at moderate ζ ($\zeta \approx 3.3$ in Fig.12(a)) yields tumbling vesicles with significant drifts, and typically between 4 and 5 spikes (in ϕ) on X. However, the tetrahedral breather PO1 is again stable in cDNS, and cDNS at larger ζ "typically" yields convergence to (stable) steady states.

As already said, we find the single morphogen ϕ mechanochemical model to be the simplest of its kind. Models that couple X to several chemical species such as Brusselators, or reaction diffusion models involving several different Min proteins, should be only slightly more complicated both theoretically and computationally, but naturally the parameter space becomes larger. Moreover, our motivating Fig.1 comes from experiments which call for bulk–surface models, in which oscillatory reactions in the fluid bulk play an important role. Such models can in principle also be studied in our setup, see, e.g., [Uec21, Ch.10] for examples with fixed domains, but for dynamic domains the

[13] We also ran cDNS with constraints for rotations and multiplier ρ, yielding the same results. Moreover, we ran cDNS in a simple implicit Euler version, and with the more elaborate high-order and adaptive code `RADAU`, obtaining essentially identical results as long as solutions do not tend to self–intersection.

compatible motion of bulk and surface mesh points still needs further software development.

In any case, we believe the bifurcation and continuation framework developed here (augmented by DNS for stability) to be crucial to get an overview of (relative) steady states and POs for the mechanochemical models (2) and (3), and similarly for the possibly more complicated models just indicated.

A Some calculus

A.1 Linearization

For $\gamma \subset \mathbb{R}^2$ a smooth, closed, parameterized (not necessarily by arc-length) curve, and $F(\gamma)$ an expression on some (Sobolev space) $H^r(\gamma)$, we calculate the derivative via

$$\partial_u F(\gamma)u = \frac{\partial}{\partial\delta} F(\gamma + \delta u\nu)\Big|_{\delta=0},$$

with expressions evaluated at $\delta = 0$ if no argument is explicitly written. A key component is the derivative of the metric $g = \langle \partial_s\gamma, \partial_s\gamma\rangle$ given by

$$\partial_u g = 2\langle \partial_s(u\nu), \partial_s\gamma\rangle = 2\sqrt{g}\,\langle \partial_s\nu, \tau\rangle\, u = -2g\kappa u,$$

using $\partial_s\nu = -\kappa\sqrt{g}\tau$. By the chain rule, we obtain

$$\partial_u\sqrt{g} = -\sqrt{g}\kappa u.$$

Since the Laplace–Beltrami operator $\Delta f = g^{-1/2}\partial_s(g^{-1/2}\partial_s f)$ depends on the metric, its derivative is computed using $\partial_u g^{-1/2} = g^{-1/2}\kappa u$ and the chain rule as

$$\partial_u\Delta f = \partial_u(g^{-1/2})\partial_s g^{-1/2}\partial_s f + g^{-1/2}\partial_u(\partial_s g^{-1/2}\partial_s f) = \kappa(\Delta f)u + g^{-1/2}\partial_s(\kappa g^{-1/2}u\partial_s f).$$

Applying the product rule to the last term we arrive at

$$\partial_u\Delta f = 2\kappa(\Delta f)u + \langle \nabla(\kappa u), \nabla f\rangle,$$

where $\nabla f = (g^{-1/2}\partial_s f)\tau$. To linearize the curvature $\kappa = \langle \Delta\gamma, \nu\rangle$ we use the previous results and find

$$\partial_u\Delta\gamma = -(\Delta u + \kappa^2 u)\nu,$$

and consequently $\partial_u\kappa = -(\Delta u + \kappa^2 u)$.

We can now write the full linearization of (3) in the normal direction, as the remaining dependencies are simple polynomials. However, we first display our setup of the 4th order Helfrich flow in (3) as a 2–component 2nd order system.[14] With $\kappa = \langle \Delta\gamma, \nu\rangle$ and $U = (u, \kappa, \phi, \lambda)$ we obtain

$$\mathcal{M}\partial_t U = \begin{pmatrix} -\mathcal{G}(U) \\ q_L(u) \end{pmatrix} = \begin{pmatrix} -\Delta(\kappa - c_0) + \frac{1}{2}\kappa(\kappa + c_0)(\kappa - c_0) - \lambda\kappa \\ -\kappa + \langle \Delta\gamma, \nu\rangle\, u \\ D\Delta\phi - \delta\phi + \zeta\frac{f(\kappa)}{\omega + f(\kappa)} \\ q_L(u) \end{pmatrix}, \quad \mathcal{M} = \begin{pmatrix} \frac{1+u}{g^{1/2}(u)} & & & \\ & 0 & & \\ & & 1 & \\ & & & 0 \end{pmatrix}, \quad (21)$$

[14] So called mixed formulation, unproblematic here because we have no boundary; see also [SGJW22] for more general cases in the geometric setting.

where $q(u) = L(\gamma + u\nu) - L_0 = 0$, and then

$$\partial_{(u,\kappa,\phi)}\mathcal{G}\psi = \begin{pmatrix} -2\kappa(\Delta(\kappa - c_0))\psi_u - \langle\nabla(\kappa\psi_u), \nabla(\kappa - c_0)\rangle & -\Delta\psi_\kappa - \frac{1}{2}(3\kappa^2 - c_0^2)\psi_\kappa & \beta(\Delta\psi_\phi + \kappa c_0\psi_\phi) \\ -\Delta\psi_u - |v|^2\psi_u & \psi_\kappa & 0 \\ 2\kappa(\Delta\phi)\psi_u + \langle\nabla(\kappa\psi_u), \nabla\phi\rangle & \zeta\omega\frac{\partial_\kappa f}{(\omega+f)^2}\psi_\kappa & \Delta\psi_\phi - \delta\psi_\phi \end{pmatrix}$$

where

$$\partial_\kappa f(\kappa) = (1 + \exp((\kappa - \kappa_0)\chi))^{-1}\exp((\kappa - \kappa_0)\chi). \tag{22}$$

Importantly, this analytical Jacobian (instead of just numerical Jacobians) is also used and very helpful in the numerics, for speed and accuracy.

A.2 Phase conditions

The equations (8) and hence (21) are purely intrinsic wrt the curve γ, and hence normal perturbations that move γ in the ambient space $\mathbb{R}^2$ are neutral directions, namely translations and rotations, aka rigid body motions. For the numerical continuation of steady states we have to take care of these neutral direction, as they appear as eigenvectors to zero eigenvalues of the Jacobian. Let $m \in C^\infty(\mathbb{R}, \mathbb{R}^2)$ be a curve with $m(0) = 0$, and let $\imath \in C^\infty(\mathbb{R}, \mathbb{R}^{2\times 2})$ be a curve of rotation matrices with $\imath(0) = 1$. They act on γ as

$$T_{m(z)}\gamma = \{p(s) + m(z) : s \in [0, 2\pi)\} \quad \text{and} \quad R_\vartheta\gamma = \{\imath(\vartheta)\gamma(s) : s \in [0, 2\pi)\}. \tag{23}$$

T_m and R_ϑ then form two dimensional respectively one dimensional Lie groups, as the tangent space at the identity $\partial_z|_{z=0}T_{m(z)}\gamma = m'(0)$ is two dimensional, and $\partial_\vartheta|_{\vartheta=0}R_\vartheta\gamma = \begin{pmatrix} -\gamma_2 \\ \gamma_1 \end{pmatrix}$ is one dimensional. As the Helfrich energy $\mathcal{H}$ and the ϕ dynamics are intrinsically defined on γ, the stationary equation $0 = \mathcal{G}(\gamma, \phi)$ is equivariant under the group generated by $\{T_m, R_\vartheta\}$ with the composition as operation. Letting

$$q_1(u) = \int_\gamma \langle e_1, u\,\nu\rangle \,\mathrm{d}s, \quad q_2(u) = \int_\gamma \langle e_2, u\,\nu\rangle \,\mathrm{d}s, \quad q_3(u) = \int_\gamma \left\langle \begin{pmatrix} -\gamma_2 \\ \gamma_1 \end{pmatrix}, u\nu \right\rangle \mathrm{d}s \tag{24}$$

with the $\mathbb{R}^2$ scalar product $\langle\cdot,\cdot\rangle$, and introducing Lagrange multipliers τ_x, τ_y and ρ for the two positional and one rotational constraints, we add $\tau_x q_1(u) + \tau_y q_2(u) + \rho q_3(u)$ to $\mathcal{H}$. Because the constraints are linear in u, we obtain the Euler Lagrange equation

$$M\partial_t \begin{pmatrix} u \\ \phi \end{pmatrix} = \mathcal{G}(u, \phi) + \begin{pmatrix} \tau_x \langle e_1, \nu\rangle + \tau_y \langle e_2, \nu\rangle + \rho(\gamma_1\nu_2 - \gamma_2\nu_1) \\ 0 \end{pmatrix} \tag{25}$$

as the equation for relative equilibria, aka the comoving frame equation, together with the constraints $(q_1, q_2, q_3)(u) = 0$, and the length constraint $q_L(u) = L(\gamma_0 + uN) - L_0 = 0$. Because all these constraints do not explicitly depend on the Lagrange multipliers, they all give DAEs of (differentiation) index 2. As only u depends on time in the constraints, their time derivative gives a linear algebraic system for the Lagrange multipliers

$$\begin{pmatrix} \langle\partial_u q_1, \partial_u q_1\rangle_{L^2} & \langle\partial_u q_1, \partial_u q_2\rangle_{L^2} & \langle\partial_u q_1, \partial_u q_3\rangle_{L^2} \\ \langle\partial_u q_2, \partial_u q_1\rangle_{L^2} & \langle\partial_u q_2, \partial_u q_2\rangle_{L^2} & \langle\partial_u q_2, \partial_u q_3\rangle_{L^2} \\ \langle\partial_u q_3, \partial_u q_1\rangle_{L^2} & \langle\partial_u q_3, \partial_u q_2\rangle_{L^2} & \langle\partial_u q_3, \partial_u q_3\rangle_{L^2} \end{pmatrix} \begin{pmatrix} \tau_x \\ \tau_y \\ \rho \end{pmatrix} = - \begin{pmatrix} \langle\mathcal{G}_1(U), \partial_u q_1\rangle_{L^2} \\ \langle\mathcal{G}_1(U), \partial_u q_2\rangle_{L^2} \\ \langle\mathcal{G}_1(U), \partial_u q_3\rangle_{L^2} \end{pmatrix},$$

by using the chain rule and with for example $\langle\partial_u q_1, \partial_u q_2\rangle_{L^2} = \int_\gamma \nu_1\nu_2 \,\mathrm{d}s$. Like for λ after (8), in principle this can be solved for (τ_x, τ_y, ρ) as long u is not too large, but here we just append (q_1, q_2, q_3)

to q_L and extend the dynamical mass matrix $\mathcal{M}$ from (21) by three zero rows.

In summary, for constant nonzero multipliers τ_x, τ_y or ρ, a steady state of (25) has some net rigid body motion in the lab-frame. Similarly, for POs $t \mapsto (\gamma(t), \phi(t))$ we want the constraints (24) (and $q_L(u) = 0$) to hold at every t. Hence let $\xi \in \Gamma$ and $\gamma = \xi_{-\eta(t)} \cdot \tilde{\gamma}$ with a function $\eta(t)$, meaning a translation of $\tilde{\gamma}$ in e_1 or e_2 direction, or a rotation by $-\eta(t)$. Then

$$\langle \gamma_t, \nu \rangle = \langle -\eta'(t)\partial_z|_{z=0}\xi_z \cdot \tilde{\gamma} + \tilde{\gamma}_t, \nu \rangle = -\eta'(t) \langle \partial_z|_{z=0}\xi_z \cdot \tilde{\gamma}, \nu \rangle + \langle \tilde{\gamma}_t, \nu \rangle .$$

Dropping the $\tilde{\cdot}$, the PCs for the dynamical problem can be considered via (25), now with τ_x, τ_y and ρ time depending as the derivatives of the corresponding $-\eta(t)$. Examples of nonzero periodic τ_x, τ_y and ρ are given in Fig.6(c), and Fig.8(b), which give relative POs, for which we then reconstruct the path of the center of mass in the lab-frame.

All of these remarks hold analogously in 2D, where however we have to deal with three translational and two rotational rigid body motions.

A.3 Amplitude equations

The linearization of (12) at $\mathbb{S}^1$ with $\lambda = \frac{1}{2}(\alpha^2 - 1)$, i.e., $(u, \phi) = (0, 0)$, yields $\partial_t U = \mathcal{L}(\partial_s, \Lambda)U$ with

$$\mathcal{L}(\partial_s, \Lambda) = \begin{pmatrix} -(\partial_s + 1)^2(\partial_s - 1)^2 & \beta(\partial_s^2 - \alpha) \\ \frac{\zeta}{2\omega}(\partial_s^2 - 1) & -D\partial_s^2 - \delta \end{pmatrix}, \tag{26}$$

and the ansatz $U(x, t) = \exp(t\mu)e_m\Phi$ with $e_m = \exp(\mathrm{i}ms)$, $m \in \mathbb{Z}$, and solving for $\mathrm{Re}(\mu) = 0$ yields (16), i.e., $\zeta_c = \dfrac{2\omega(m-1)(m+1)(m^2D^2 + \delta)}{(m^2 - \alpha)\beta}$, with eigenvector

$$\Psi_c = \begin{pmatrix} 1 \\ \frac{(m+1)^2(m-1)^2}{\beta(m^2-\alpha)} \end{pmatrix} e_m.$$

Here we briefly explain the amplitude formalism for branches bifurcating at ζ_c, and how that depends on our smoothing parameter χ in (5).

Due to the $O(2)$ symmetry of the system, BPs on $\mathbb{S}^1$ are double, but with the "hidden $\mathbb{Z}_2$ symmetry" of rotation by $\pi/(2m)$, which makes all bifurcations pitchforks. To derive the amplitude equations for these bifurcations, let $\zeta = \zeta_c + \varepsilon^2\tilde{\zeta}$, introduce the slow time scale $T = \varepsilon^2 t$, let $A = A(T)$, and set

$$U(s, t) = \varepsilon\Psi_A(s, t) = \varepsilon A(T)\Psi_c(s) + \varepsilon^2 \left(\frac{1}{2}\Phi_0 e_0 + \Phi_2 e_{2m} + \text{c.c.} \right) + \text{h.o.t.} \tag{27}$$

We expand the right hand side of (12) as

$$\mathcal{G}(U) = \mathcal{L}(\partial_s, \Lambda)U + B[U, U] + C[U, U, U] + \mathcal{O}(\|U\|^4), \tag{28}$$

with symmetric bilinear form $B[U, U] = \dfrac{1}{2}\left(\partial_u^2\mathcal{G} + \partial_{u\phi}^2\mathcal{G} + \partial_{\phi u}\mathcal{G} + \partial_\phi^2\mathcal{G}\right)[U, U]$, and symmetric trilinear form $C[U, U, U] = \frac{1}{6}\left(\partial_u^3\mathcal{G} + 3\partial_{uu\phi}^3\mathcal{G} + 3\partial_{u\phi\phi}^3\mathcal{G} + \partial_\phi^3\mathcal{G}\right)[U, U, U]$, and similarly the constraint as

$$L(\gamma) - L_0 = \int_{\mathbb{S}^1} \partial_u L(0)u \, \mathrm{d}s + \int_{\mathbb{S}^1} B_L(u, u) \, \mathrm{d}s + \mathcal{O}(\|u\|^4). \tag{29}$$

We do not display here the formulas for B, C and B_L which become cumbersome, see [MU26b], but

note that $(\partial_u^2\mathcal{G}(u_1,u_2))_2 = \frac{\zeta}{\omega^2}(\omega\partial_\kappa^2 f(0)\partial_u^2\kappa - 2\partial_u f(0)^2)u_2(s)u_1(s)$ with $\partial_\kappa f(\kappa)$ from (22) and

$$\partial_\kappa^2 f(\kappa) = \frac{\chi \mathrm{e}^{\chi(\kappa-\kappa_0)}}{\left(\mathrm{e}^{\chi(\kappa-\kappa_0)}+1\right)^2}. \tag{30}$$

Similarly $\partial_\kappa^k f(\kappa) \sim \chi^{k-1}$, i.e., the higher derivatives become more and more singular with growing χ. Inserting $\varepsilon\Psi_A$ in (12), all $O(\varepsilon)$ terms vanish by construction, and at order ε^2 we obtain

$$0 = \mathcal{L}(0,\Lambda_c)\Phi_0 + 2|A|^2\hat{B}[\Psi_c,\overline{\Psi}_c] + \tilde{\lambda}\begin{pmatrix}1\\0\end{pmatrix}, \tag{31a}$$

$$0 = \mathcal{L}(i2m,\Lambda_c)\Phi_2 + A^2\hat{B}[\Psi_c,\Psi_c], \tag{31b}$$

$$0 = \partial_u L(0)(\Phi_0)_1 + |A|^2\hat{B}_L[(\Psi_c)_1,(\overline{\Psi}_c)_1], \tag{31c}$$

with $\mathcal{L}(i2m,\Lambda_c)$ from (15), and where $\hat{B}[\cdot,\cdot] = \mathcal{F}B[\cdot,\cdot]$. From the dispersion relation for (15) we can solve (31) for $\Phi_0,\Phi_2 \in \mathbb{C}^2$ and $\tilde{\lambda} \in \mathbb{R}$.

In order to remove $\varepsilon^3 e_m$ terms we need to solve

$$\mathcal{L}(im,\Lambda_c)\tilde{\Psi} = -\partial_T A\Psi_c + \partial_\zeta\mu_c\Psi_c + 2AB[\Psi_c,\Phi_0] + 2\overline{A}B[\overline{\Psi}_c,\Phi_2 e_{2m}] + 3C[\Psi_c,\Psi_c,\Psi_c] + \tilde{\lambda}\partial_u\kappa\begin{pmatrix}1\\0\end{pmatrix}.$$

As $\mathcal{L}(m,\Lambda_c)$ is not invertible, we get the solvability condition from the Fredholm alternative that

$$\partial_T A = \tilde{\zeta}\nu_1 A + \nu_2 A + \nu_3\overline{A} + \nu_4|A|^2A + A\tilde{\lambda}\partial_u\kappa, \tag{32}$$

where $\nu_1 = \partial_\zeta\mu_c$, $\nu_2 = 2\left\langle \hat{B}[\Psi_c,\Phi_0],\Phi_c^*\right\rangle$, $\nu_3 = 2\left\langle \hat{B}[\overline{\Psi}_c,\Phi_2 e_{2m}],\Phi_c^*\right\rangle$, $\nu_4 = 3\left\langle \hat{C}[\Psi_c,\Psi_c,\overline{\Psi}_c],\Phi_c^*\right\rangle$. Here $\hat{C}[\cdot,\cdot,\bar{\cdot}] = \mathcal{F}C[\cdot,\cdot,\bar{\cdot}]$, and

$$\Phi_c^* = \begin{pmatrix} 1 \\ \frac{(m^2-\alpha)\beta}{(m^4+(D-2)m^2+\delta+1)} \end{pmatrix}$$

is the eigenvector to the adjoint eigenvalue problem $\mathcal{L}^*(m,\Lambda_c)\Phi_c^* = \overline{\mu}_c\Phi_c^*$, and so that $\langle\Phi_c^*,\Phi_c\rangle = 1$. In (32), we explicitly kept ν_3 because $\hat{B}$ involves s–derivatives and hence $\Phi_2 e_{2m}$ must be used for ν_3, not just Φ_2. However, as $\nu_2,\tilde{\lambda} \sim |A|^2$ and $\nu_3 \sim A^2$ we get the normal form amplitude equation for a pitchfork

$$\partial_T A = \tilde{\zeta}\nu_1 A + \tilde{\nu}|A|^2A.$$

To find steady nontrivial branches bifurcating at ζ_c, we can now solve (32) for steady states, i.e., solve $\tilde{\zeta}\nu_1 A + \tilde{\nu}|A|^2A = 0$ for A. However, the quality of the prediction by the amplitude equation heavily depend on the value of χ. From (30), the quadratic terms depend on χ and the cubic terms on χ^2. This couples via ν_2 and ν_3 in the cubic coefficient in the amplitude equation. For the parameters $(\alpha,\beta,D,\delta,\omega) = (0.7,1,0.1,0.3,1)$ we compare in Fig.14 the predictions of the amplitude equations with the numerical continuation for different values of χ. For small χ, the curvature of f_χ at $\kappa = 1$ is small and the approximation of the max function rather poor. For $\chi = 5$, the numerical values in (32) are

$$\mathcal{W}_2: \quad \partial_T A = 0.51A\tilde{\zeta} - 19.85|A|^2A, \tag{33a}$$

$$\mathcal{W}_3: \quad \partial_T A = 0.51A\tilde{\zeta} - 244.33|A|^2A. \tag{33b}$$

In this case, the bifurcations are supercritical and the predictions by the amplitude equations for ϕ and also for the Lagrange multiplier are rather accurate also at $\mathcal{O}(1)$ amplitude. In contrast, for

higher $\chi = 50$, the amplitude equations are

$$\mathcal{W}_2: \quad \partial_T A = 0.51 A\tilde{\zeta} + 583.4|A|^2 A, \tag{34a}$$

$$\mathcal{W}_3: \quad \partial_T A = 0.51 A\tilde{\zeta} + 5708.38|A|^2 A. \tag{34b}$$

From (34), the bifurcations are now subcritical. This also holds for our numerical bifurcations, but with a fold shortly after the bifurcation point, and for large χ the approximation by the AEs is therefore only good close to bifurcation.

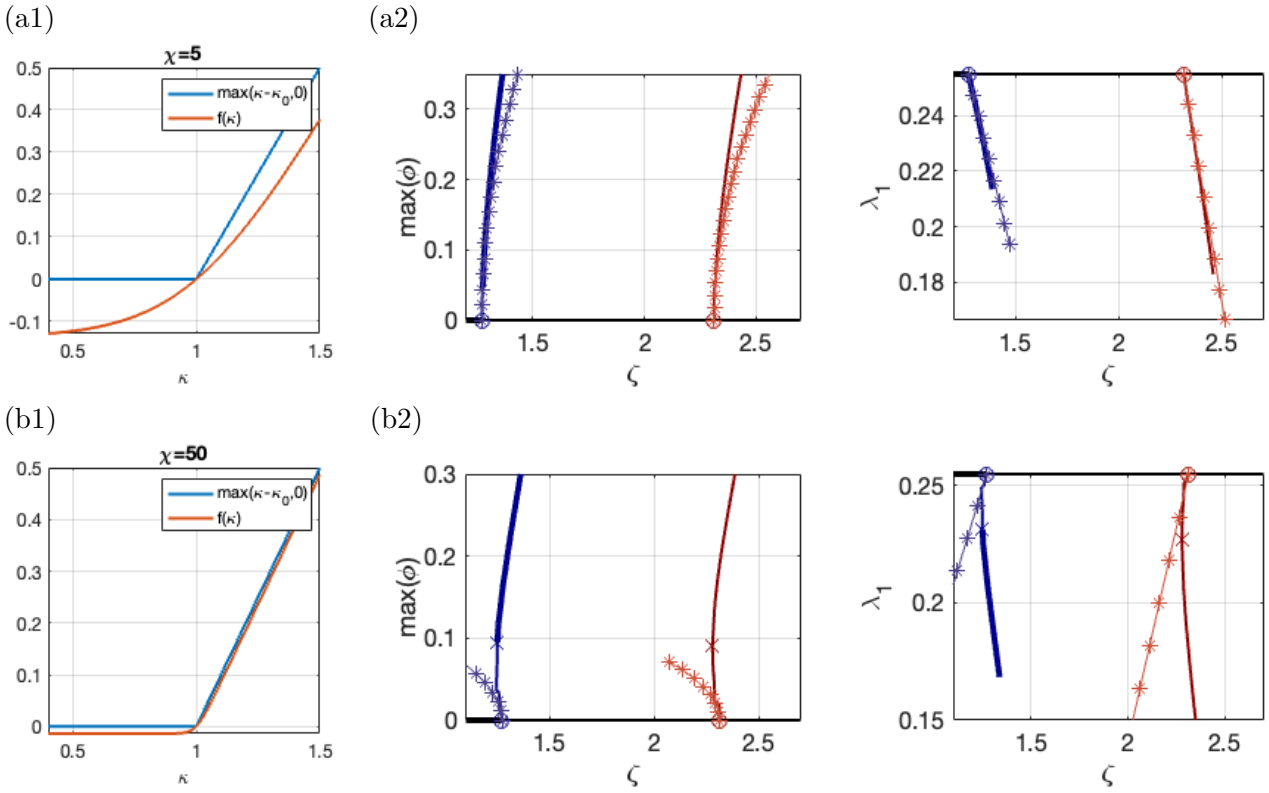

Figure 14: Comparison of the numerical continuation (lines) and the amplitude prediction (dotted lines) for $\chi = 5$ in (a) and $\chi = 50$ in (b) for the parameters $(\alpha, \beta, D, \delta, \omega,) = (0.7, 1, 0.1, 0.3, 1)$.

In summary, for any $\chi > 0$, the AEs (32) can be justified by standard center manifold theory, but the range of validity, i.e., the maximal allowed ε in (27) shrinks with $\chi \to \infty$. However, the choice of χ does not seem to have much influence on the global behavior of the nontrivial steady state branches $\mathcal{W}_m$; this is expected as for nontrivial solutions, κ is bounded away from 1 on most of γ. A rather ambitious but interesting next step would be to study the local bifurcations from $\mathbb{S}^1$ in the singular limit $\chi \to \infty$, where standard bifurcation theory does not apply. See also Remark 2.1.

B Numerical algorithms

The `Xcont` extension [MU24a, MU24b] of `pde2path` provides methods for the numerical continuation and bifurcation analysis of manifolds as solutions of geometric PDEs. The focus so far were steady 2D problems, but the algorithms also apply to the 1D case, see the introduction of [Mei24]. Some further features needed here pertain to PO continuation, explained below, after first briefly recalling the geometry setting of the `Xcont` extension, in 1D.

B.1 Spatial and temporal discretization

We spatially discretize a closed curve γ into $\mathtt{n_t}$ linear connections $(\mathtt{tri})_{i=1}^{\mathtt{n_t}}$ with $\mathtt{n_p} = \mathtt{n_t}$ nodes $(\mathtt{g}_j)_{j=1}^{\mathtt{n_p}}$, ordered such that the two neighbors of $\mathtt{g_j}$ are $\mathtt{g_{i-1}}$ and $\mathtt{g_{i+1}}$ (with $\mathtt{g_0} = \mathtt{g_{np}}$ and $\mathtt{g_{np+1}} = \mathtt{g_1}$ implied). Using piecewise linear hat functions ψ_j, with $\psi_j(\mathtt{g}_k) = \delta_{jk}$, the weak form of the Laplace–Beltrami operator is given by

$$L_{jk} = -\int_\gamma \langle \nabla\psi_j, \nabla\psi_k \rangle \, \mathrm{d}s,$$

where $\nabla f = (\partial_s f)\tau$ is the curve gradient. Instead of the standard mass matrix $M_{jk} = \int_X \psi_j \psi_k \, \mathrm{d}S$, as in [MU24b] we use the (diagonal, lumped) Voronoi mass matrix, which in 1D simply reads

$$M_{jj} = \frac{1}{2}\left(\|\mathtt{g_j} - \mathtt{g_{j-1}}\|_2 + \|\mathtt{g_{j+1}} - \mathtt{g_j}\|_2\right). \tag{35}$$

Then we discretize κ in the weak FEM formulation as $M\mathtt{k} = \langle L\mathtt{g}, \nu\rangle$, where ν is the vertex normal computed as the average of the two adjacent face normals, weighted by element size. The implementation uses the `gptoolbox` [Jac24], see also [MU24b] for comments on convergence rates (in 2D). Finally, we discretize the mixed formulation (21) in a standard fashion, i.e.,

$$\begin{pmatrix} M & & \\ & 0 & \\ & & M \end{pmatrix} \begin{pmatrix} \langle \dot{\mathtt{g}}, \nu\rangle \\ \dot{\mathtt{k}} \\ \dot\phi \end{pmatrix} = -\tilde{\mathtt{G}}(u, \mathtt{k}, \phi) = -\begin{pmatrix} L(\mathtt{k} - c_0) + M\big(\frac{1}{2}\mathtt{k}\big(\mathtt{k} + c_0\big)\big(\mathtt{k} - c_0\big) - \lambda\mathtt{k}\big) \\ \langle L\mathtt{g}, \nu\rangle - M\mathtt{k} \\ -L\phi + M\left(\delta\phi - \zeta\frac{f(\mathtt{k})}{\omega + f(\mathtt{k})}\right) \end{pmatrix}, \tag{36a}$$

together with the (discretized) length constraint

$$q_L(u) = L(\mathtt{g}) - \mathtt{L_0} = \mathtt{0}, \tag{36b}$$

which determines the Lagrange multiplier λ, and similar discretizations of the phase conditions $(q_1, q_2, q_3)(u) = 0$, and with then adding (the discretizations of) $\tau_x \langle e_1, \nu\rangle + \tau_y \langle e_2, \nu\rangle + \rho(\gamma_1\nu_2 - \gamma_2\nu_1)$ from (25) to the first line of the rhs of (36a).

Steady state continuation. Steady states can now be continued in parameters as solutions of

$$0 = -\tilde{\mathtt{G}}(u, \mathtt{k}, \phi; \Lambda), \qquad q_L(u) = 0, \tag{37}$$

where $\Lambda \in \mathbb{R}^p$ is a generic name for the pertinent *active* parameters, e.g., $\Lambda = (\zeta, \lambda)$ with ζ the *primary active* parameter here, and λ as secondary active parameter. However, due to the translational and rotational invariance of (3) and hence approximate[15] invariances of (38), as explained above we need phase conditions $q_{\text{phase}}(\gamma, \phi, \Lambda) = 0$ and associated Lagrange multipliers as further secondary active parameters, see §A.2, and for the system thus obtained we write

$$0 = -\tilde{\mathtt{G}}(u, \mathtt{k}, \phi; \Lambda), \qquad q(u) = 0. \tag{38}$$

Now assume we have a point

$$U_0 = (\gamma(\sigma_0), \kappa(\sigma_0), \phi(\sigma_0), \Lambda(\sigma_0)) \tag{39}$$

on a solution branch $(\sigma_-, \sigma_0] \ni \sigma \mapsto U(\sigma)$ (with a slight abuse of notation explained below writing $\gamma(\sigma_0)$ instead of $u(\sigma_0)$ for the first component of U) and a unit (in some suitable weighted norm)

[15] the discretization already breaks these invariances, but only very weakly and in an uncontrolled way

tangent

$$\Upsilon(\sigma_0) = \partial_\sigma U(\sigma_0) = (\Upsilon_\gamma, \Upsilon_\kappa, \Upsilon_\phi, \Upsilon_\Lambda) \tag{40}$$

to that solution branch, and a step length $\mathrm{d}\sigma$.[16] Then we make a predictor

$$U(\sigma) = U(\sigma_0) + \mathrm{d}\sigma\Upsilon(\sigma_0) \tag{41}$$

at $\sigma = \sigma_0 + \mathrm{d}\sigma$, and aim to solve (38) for $(u, \kappa, \phi, \Lambda)$ by Newton loops, starting with $u^0 = 0$, in the hyperplane orthogonal to Υ, which is the crucial idea of arclength (here σ) continuation to deal with folds. In case of success we update $\gamma(\sigma) = \gamma(\sigma_0) + u(\sigma)\nu(\sigma_0)$ and go to the next step, which we summarize in short as `updX` (as the name of the pertinent function in `Xcont`, "update X", in 1D $X = \gamma$); otherwise, a standard idea is to reduce the step length $\mathrm{d}\sigma$ and try again, and altogether the convergence speed (or failure) of the Newton loops is a basis for stepsize control. Thus, u is always small in this setup and only meaningful together with the "current" base manifold $\gamma(\sigma_0)$, which is why we write $\gamma(\sigma_0)$ in (39).

PO continuation. To continue POs, we also need a temporal discretization of (37). To compute a PO with (unknown) period T, we consider the boundary value problem rescaled to the temporal interval $[0, 1]$, i.e.,

$$\begin{pmatrix} M & & \\ & 0 & \\ & & M \end{pmatrix} \begin{pmatrix} \langle \dot{\mathtt{g}}, \nu \rangle \\ \dot{\mathtt{k}} \\ \dot{\phi} \end{pmatrix} + T\tilde{\mathtt{G}}(u, \mathtt{k}, \phi) = 0, \tag{42a}$$

together with the periodicity condition

$$(u(0), \mathtt{k}(0), \phi(0), \Lambda(0)) = (u(1), \mathtt{k}(1), \phi(1), \Lambda(1)), \tag{42b}$$

where we already preview that at least some of the Lagrange-multipliers, namely λ, are dynamic, i.e., functions of t. For a discretization $0 = t_0, t_1, \ldots, t_{m-1} \in [0, 1)$ with stepsize $h_j = t_{j+1} - t_j$ and periodicity condition $U(t_m) = U(t_0)$, we discretize the temporal derivative of the Helfrich equation as $\langle \dot{\mathtt{g}}(t_j), \nu(t_j) \rangle \approx \left\langle h_j^{-1}(\mathtt{g}(t_j) - \mathtt{g}(t_{j-1})), \nu(t_j) \right\rangle$, and use a mid point approximation of the first and third component of $\tilde{G}$, i.e., $\tilde{G}_i(t_j) = \frac{1}{2}(\tilde{G}(t_j) + \tilde{G}(t_{j-1}))$, but evaluate the second component for the elliptic equation $\langle Lg, \nu \rangle - Mk = 0$, and the constraints, at t_j. In the numerical continuation of POs, the updating procedure of γ is as follows: The current γ is given by the field `p.hopf.X`, and the new γ at time slice t_j is $\mathtt{Xn}(j) = \mathtt{p.hopf.X}(:, :, j) + \mathtt{u}(:, j)\nu(j)$. The temporal discretization of $\langle \dot{\mathtt{g}}, \nu \rangle$ in the first line of (42a) then is

$$\langle \dot{\mathtt{g}}(t_j), \nu(t_j) \rangle \approx \left\langle h_j^{-1}(\mathtt{Xn}(t_j) - \mathtt{Xn}(t_{j-1})), \nu(t_j) \right\rangle. \tag{43}$$

DNS and cDNS. In DNS, we do one time step of length h and then update γ, and hence (43) simplifies to

$$\begin{aligned} \langle \dot{\mathtt{g}}(t+h), \nu(t+h) \rangle &\approx \left\langle h^{-1}(\mathtt{g}(t+h) - \mathtt{g}(t)), \nu(t+h) \right\rangle = \left\langle h^{-1}(\mathtt{g}(t) + u\nu(t) - \mathtt{g}(t)), \nu(t+h) \right\rangle \\ &= h^{-1} \langle \nu(t), \nu(t+h) \rangle u. \end{aligned} \tag{44}$$

Due to the length constraint $q_L(u) = 0$ we have a differential algebraic equation (DAE) of (differentiation) index 2, where the Lagrange multiplier λ is a time dependent part of the solution. With

[16] The default name for the (dummy) arclength parameter in continuation problems is s, see [Uec21], also in our `Xcont` setting [MU24b]; however, for the 1D problem we already use s as the parametrization of γ. Also note that the branch $\sigma \mapsto U(\sigma)$ always means a branch of curves γ, fields ϕ and (active) parameters Λ.

$\eta(t) := \langle \nu(t-h), \nu(t) \rangle$ we write the full DAE system as

$$\begin{pmatrix} M\eta(t) & & & \\ & 0 & & \\ & & M & \\ & & & 0 \end{pmatrix} \begin{pmatrix} \dot{u}(t) \\ \dot{\mathtt{k}}(t) \\ \dot{\phi}(t) \\ \dot{\lambda}(t) \end{pmatrix} + \begin{pmatrix} \tilde{\mathtt{G}}_1(u(t), \mathtt{k}(t), \phi(t), \lambda(t)) \\ \tilde{\mathtt{G}}_2(u(t), \mathtt{k}(t), \phi(t), \lambda(t)) \\ \tilde{\mathtt{G}}_3(u(t), \mathtt{k}(t), \phi(t), \lambda(t)) \\ q_L(u(t)) \end{pmatrix} = \begin{pmatrix} 0 \\ 0 \\ 0 \\ 0 \end{pmatrix}, \tag{45}$$

where again the $\dot{(\cdot)}$ stands for the discretization of the time derivative, and $\dot{\lambda}$ and $\dot{\mathtt{k}}$ only appear formally in (45) to visualize the structure. We call (45) with $\tau_x, \tau_y, \rho = 0$ the lab–frame formulation of the DAE (where the 2nd row of (45) has differentiation index 1 and the last row index 2), and the associated numerical integration simply DNS, see below.

Alternatively, including the positional constraints q_1, q_2, q_3 from (24),(25) in the DNS yields DAEs for (τ_x, τ_y, ρ) of index 2. We write this as

$$\begin{pmatrix} M\eta(t) & & & & \\ & 0 & & & \\ & & M & & \\ & & & 0 & \\ & & & & 0_p \end{pmatrix} \begin{pmatrix} \dot{u}(t) \\ \dot{\mathtt{k}}(t) \\ \dot{\phi}(t) \\ \dot{\lambda}(t) \\ \dot{\Lambda}_p \end{pmatrix} + \begin{pmatrix} \tilde{\mathtt{G}}_1(u(t), \mathtt{k}(t), \phi(t), \Lambda(t)) \\ \tilde{\mathtt{G}}_2(u(t), \mathtt{k}(t), \phi(t), \Lambda(t)) \\ \tilde{\mathtt{G}}_3(u(t), \mathtt{k}(t), \phi(t), \Lambda(t)) \\ q_L(u(t)) \\ q_p(u(t)) \end{pmatrix} = \begin{pmatrix} 0 \\ 0 \\ 0 \\ 0 \\ 0 \end{pmatrix} \tag{46}$$

where $q_p(u(t)) = (q_1, q_2, q_3)(u(t))$, $0_p = 0 \in \mathbb{R}^{3\times 3}$, and $\Lambda_p = (\tau_x, \tau_y, \rho)$, or, dropping the rotational constraint $q_p(u(t)) = (q_1, q_2)(u(t))$, $0_p = 0 \in \mathbb{R}^{2\times 2}$, and $\Lambda_p = (\tau_x, \tau_y)$, and we call (46) constrained DNS (cDNS). The idea of using (46) instead of (45) for DNS is to trade drift (and rotation) in the lab frame for time–dependent non–zero τ_x, τ_y (and ρ), which turns out to be a more robust formulation as it seems to avoid the accumulation of numerical errors in the rigid motion neutral modes.

There are several numerical strategies for DAEs, see for example [HLR89, HW96]. A simple method for (45) and (46) is implicit Euler such that the 2nd and 4th row in (45) (and the 5th row in (46)) simply yield constraints at t_{j+1}, and we take this as a our basic strategy. However, implicit Euler is only first order in $h = t_{j+1} - t_j$, and can be "overdamping" and hence in particular be inadequate for approximating POs. See, e.g., the discussion of the mathematical pendulum in Cartesian coordinates as (index 1,2, or 3) DAE in [HLR89]. Therefore we checked our implicit Euler results for (45) and (46) against the high–order adaptive code `RADAU`. The results fully agree for stable POs and for the convergence of DNS to stable steady states, but for unstable dynamics (trigger waves, and cases that lead to self–intersection and blowup) significant differences can occur, as `RADAU` often yields non–convergence as γ becomes strongly distorted. Thus, we mostly use `RADAU` for validation of the stable dynamics, and, moreover, the 2D X results in §3 are all with implicit Euler as `RADAU` becomes too slow for the many degrees of freedom there, and is only used for some validations.

B.2 Mesh handling

Mesh handling is crucial in all our numerics, i.e., steady state continuation, PO continuation, and DNS: as γ changes (in time, or in continuation), the mesh may deteriorate, in particular since so far we only describe normal displacements. Basic refinement and coarsening strategies for geometric PDE's in `pde2path` are explained in [MU24a] (for the 2D case). Especially coarsening is crucial to deal with neck development. Here we additionally rely on a different type of mesh handling following [BMN05]: `tamo`=tangential mesh optimization, see Fig. 15(a) for illustration, and (b) for examples on a coarse mesh.

The key idea is to find a good approximation of the tangent space to move a point along, keeping the enclosed area fixed. We use the tangent plane (in 1D tangent line) spanned by adjacent barycen-

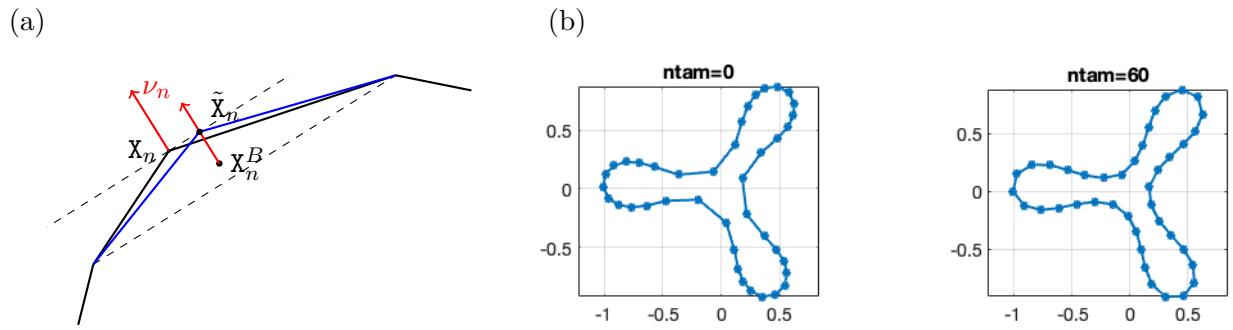

Figure 15: (a) Schematic picture of the `tamo` algorithm for constructing a the new vertex $\tilde{\mathtt{X}}_n = \mathtt{X}_n^B + \eta\nu_n$. (b) shows an exemplary use of ntam times application of `tamo.m`

ters. Let $\mathtt{X}_n$ be a vertex of the polygonal curve and $\mathcal{S}$ the "star" surrounding it (the support of the FEM basis function). In 1D, $\mathcal{S}$ is simply the two elements connecting $\mathtt{X}_{n-1}$ with $\mathtt{X}_n$ and $\mathtt{X}_{n+1}$ with $\mathtt{X}_n$. Compute the vertex normal ν_n as the weighted average of each element normal,

$$\nu_n = \frac{1}{|S_{n-1}| + |S_n|}(\nu_{S_{n-1}}|S_{n-1}| + \nu_{S_n}|S_n|),$$

which tilts towards larger elements. The barycenter of an element is $\hat{\mathtt{X}}_n = \frac{1}{2}(\mathtt{X}_n + \mathtt{X}_{n-1})$ and the averaged barycenter of a star then is $\hat{\mathtt{X}}_n^B = \frac{1}{2}(\hat{\mathtt{X}}_n + \hat{\mathtt{X}}_{n-1})$. From this we compute the new position $\tilde{\mathtt{X}}_n$ as

$$\tilde{\mathtt{X}}_n = \hat{\mathtt{X}}_n^B + \eta\nu_n,$$

where η is chosen such that the areas of triangles $(\mathtt{X}_n, \hat{\mathtt{X}}_n, \hat{\mathtt{X}}_{n-1})$ and $(\tilde{\mathtt{X}}_n, \hat{\mathtt{X}}_n, \hat{\mathtt{X}}_{n-1})$ are equal. Using that the area of a triangle (A, B, C) is $\frac{1}{2}(B - A) \times (C - A)$, we thus want $(\tilde{\mathtt{X}}_n - \hat{\mathtt{X}}_n) \times (\hat{\mathtt{X}}_{n-1} - \hat{\mathtt{X}}_n) = (\mathtt{X}_n - \hat{\mathtt{X}}_n) \times (\hat{\mathtt{X}}_{n-1} - \hat{\mathtt{X}}_n)$, and solving for η yields

$$\eta = \frac{(\mathtt{X}_n - \hat{\mathtt{X}}_n) \times (\hat{\mathtt{X}}_{n-1} - \hat{\mathtt{X}}_n) - (\hat{\mathtt{X}}_n^B - \hat{\mathtt{X}}_n) \times (\hat{\mathtt{X}}_{n-1} - \hat{\mathtt{X}}_n)}{(\nu_n - \hat{\mathtt{X}}_n) \times (\hat{\mathtt{X}}_{n-1} - \hat{\mathtt{X}}_n)}.$$

This algorithm `tamo` is fast and under some iteration (`ntam` iterations with typically `ntam` between 10 and 80) very efficient in fixing mesh distortion. Essentially the same works in 2D, in a slightly more complex fashion, and we apply `tamo` as follows:

- In steady state continuation, we apply `tamo` after each continuation step. Importantly, as ϕ lives at the mesh points, after each `tamo` step, or alternatively at the end of the `tamo` iteration, ϕ must be interpolated from the old mesh points to the new mesh points, and we call this `phii`. This is very easy in 1D, by simply using the arclength coordinates on γ and γ_{new}, but slightly more complicated and expensive in 2D. Then, after `tamo` and `phii` we run one more Newton loop to update the current solution (γ, ϕ), and then proceed to the next continuation step.
- In PO continuation, for larger amplitude POs with stronger distortion of γ, we apply `tamo` (and `phii`) at each time slice t_j, and then run a Newton loop on the full system (36).
- In DNS, we run `tamo` and `phii` after a selected number of time steps $\mathtt{n_{DNS}}$ of step size h. For slow dynamics, e.g., near steady state, $\mathtt{n_{DNS}}$ (and h) can in principle be chosen large, but in faster dynamics choosing small $\mathtt{n_{DNS}}$, in some cases $\mathtt{n_{DNS}} = 1$, is very helpful to have DNS with h bounded away from 0.

References

[BEGY23] C. Beta, L. Edelstein–Keshet, N. Gov, and A. Yochelis. From actin waves to mechanism and back: How theory aids biological understanding. *Elife*, 12:e87181, 2023.

[BMN05] E. Bänsch, P. Morin, and R. Nochetto. A finite element method for surface diffusion: the parametric case. *J. Comput. Phys.*, 203(1):321–343, 2005.

[BMRMC18] F. Brinkmann, M. Mercker, T. Richter, and A. Marciniak-Czochra. Post-Turing tissue pattern formation: Advent of mechanochemistry. *PLOS Computational Biology*, page 1006259, 2018.

[CLSL21] S. Christ, Th. Litschel, P. Schwille, and R. Lipowsky. Active shape oscillations of giant vesicles with cyclic closure and opening of membrane necks. *Soft Matter*, 17:319–330, 2021.

[DH15] S. Dharmavaram and T. J. Healey. On the equivalence of local and global area-constraint formulations for lipid bilayer vesicles. *Z. Angew. Math. Phys.*, 66(5):2843–2854, 2015.

[DP06] A.P.S. Dias and R.C. Paiva. A note on Hopf bifurcation with dihedral group symmetry. *Glasg. Math. J.*, 48(1):41–51, 2006.

[GMGOS07] A. Gomez-Marin, J. Garcia-Ojalvo, and J. M. Sancho. Self-sustained spatiotemporal oscillations induced by membrane-bulk coupling. *Phys. Rev. Let.*, 98:168303, 2007.

[GNPS96] R.E. Goldstein, P. Nelson, T. Powers, and U. Seifert. Front progagation in the pearling instability of tubular vesicles. *J.Phys.II*, 6:767–796, 1996.

[GW16] J. Gou and M. Ward. Oscillatory dynamics for a coupled membrane-bulk diffusion model with Fitzhugh-Nagumo membrane kinetics. *SIAM J. Appl. Math.*, 76(2):776–804, 2016.

[Hel73] W. Helfrich. Elastic properties of lipid bilayers: Theory and possible experiments. *Zeitschrift für Naturforschung*, 28:693, 1973.

[HLR89] E. Hairer, Ch. Lubich, and M. Roche. *The Numerical Solution of Differential-Algebraic Systems by Runge-Kutta Methods*. Springer, 1989.

[HMTB+25] J.M. Hughes, C. Martinez-Torres, C. Beta, L. Edelstein–Keshet, and A. Yochelis. A dissipative mass conserved reaction–diffusion system reveals switching between coexisting polar and oscillatory cell motility states. *Chaos*, 35:051103, 2025.

[HW96] E. Hairer and G. Wanner. *Solving ordinary differential equations. II: Stiff and differential-algebraic problems.* Springer, 1996.

[IMK+13] E. B. Isaac, U. Manor, B. Kachar, A. Yochelis, and N. Gov. Linking actin networks and cell membrane via a reaction-diffusion-elastic description of nonlinear filopodia initiation. *Phys.Rev.E*, 88:022718–1, 2013.

[Jac24] A. Jacobson. gptoolbox, `https://github.com/alecjacobson/gptoolbox`, 2024.

[KPP17] M. Koiso, B. Palmer, and P. Piccione. Stability and bifurcation for surfaces with constant mean curvature. *Journal of the Mathematical Society of Japan*, 69(4):1519 – 1554, 2017.

[LDS20] I. Levin, R. Deegan, and E. Sharon. Self-oscillating membranes: Chemomechanical sheets show autonomous periodic shape transformation. *Phys. Rev. Lett.*, 125:178001, 2020.

[Lip22] R. Lipowsky. Remodeling of membrane shape and topology by curvature elasticity and membrane tension. *Adv.Biology*, 6:2101020, 2022.

[LMFAO21] S. Lia, D. Matoz-Fernandeza, A. Aggarwal, and M. Olvera de la Cruz. Chemically controlled pattern formation in self-oscillating elastic shells. *PNAS*, 118:e2025717118, 2021.

[LRM+18] Th. Litschel, B. Ramm, R. Maas, M. Heymann, and P. Schwille. Beating vesicles: Encapsulated protein oscillations cause dynamic membrane deformations. *Angew. Chem. Int. Ed*, 57:16286–16290, 2018.

[Mat04] P. C. Matthews. Pattern formation on a sphere. In *Dynamics and bifurcation of patterns in dissipative systems*, volume 12 of *World Sci. Ser. Nonlinear Sci. Ser. B*, pages 102–123. World Sci. Publ., Hackensack, NJ, 2004.

[Mei24] A. Meiners. Differential geometric bifurcation problems – theory and applications to minimal surfaces and biomembranes, 2024. PhD thesis.

[MHMC13] M. Mercker, D. Hartmann, and A. Marciniak-Czochra. A mechanochemical model for embryonic pattern formation: Coupling tissue mechanics and morphogen expression. *PLOS ONE*, 8:1–6, 12 2013.

[MMCRH13] M. Mercker, A. Marciniak-Czochra, T. Richter, and D. Hartmann. Modeling and computing of deformation dynamics of inhomogeneous biological surfaces. *SIAM J. Appl. Math.*, 73(5):1768–1792, 2013.

[MSD18] P. Miller, N. Stoop, and J. Dunkel. Geometry of wave propagation on active deformable surfaces. *Phys. Rev. Lett.*, 120:268001, 2018.

[MU24a] A. Meiners and H. Uecker. Differential geometric bifurcation problems in `pde2path` – algorithms and tutorial examples, 2024. Available at [pde26].

[MU24b] A. Meiners and H. Uecker. Numerical continuation and bifurcation for differential geometric PDEs. *Numerical Mathematics – Theory Methods Applications*, OA-2024:0005, 2024.

[MU26a] A. Meiners and H. Uecker. Helfrich cylinders – instabilities, bifurcation analysis and amplitude equations. *SIAM J. Appl. Dyn.Systems*, 2026.

[MU26b] A. Meiners and H. Uecker. Supplementary information for *Breathing and moving vesicles in a geometric mechanochemical model*, `https://pde2path.uol.de/apps`, 2026.

[NDV25] D. Nesenberend, A. Doelman, and Fr. Veerman. Curvature induced patterns: A geometric, analytical approach to understanding a mechanochemical model, 2025. Preprint.

[Nog25] Hiroshi Noguchi. Nonequilibrium Membrane Dynamics Induced by Active Protein Interactions and Chemical Reactions: A Review. *ChemSystemsChem*, 7:e202400042, 2025.

[NY12] Takeyuki Nagasawa and Taekyung Yi. Local existence and uniqueness for the n-dimensional Helfrich flow as a projected gradient flow. *Hokkaido Math. J.*, 41(2):209–226, 2012.

[pde26] pde2path. `https://pde2path.uol.de/`, 2026.

[PLXD+20] Fr. Paquin-Lefebvre, Bin Xu, K.L. DiPietro, A.E. Lindsay, and A. Jilkine. Pattern formation in a coupled membrane-bulk reaction-diffusion model for intracellular polarization and oscillations. *J. Theoret. Biol.*, 497:110242, 23, 2020.

[RSS24] F. Rupp, C. Scharrer, and M. Schlierf. Gradient flow dynamics for cell membranes in the Canham-Helfrich model, `https://arxiv.org/pdf/2408.07493`, 2024.

[SBL90] U. Seifert, K. Berndl, and R. Lipowsky. Shape transformations of vesicles: Phase diagram. *Phys.Rev. A*, 44:1182–1202, 1990.

[Sei97] U. Seifert. Configurations of fluid membranes and vesicles. *Advances in Physics*, 46(1):13–137, 1997.

[SG11] C. Sample and A. Golovin. Morphological and chemical oscillations in a double-membrane system. *SIAM J. Appl. Math.*, 71(2):622–634, 2011.

[SGJW22] O. Stein, E. Grinspun, A. Jacobson, and M. Wardetzky. A mixed finite element method with piecewise linear elements for the biharmonic equation on surfaces, `http://arxiv.org/pdf/1911.08029`, 2022.

[SL95] U. Seifert and R. Lipowsky. Morphology of Vesicles. In R. Lipowsky and E. Sackmann, editors, *Handbook of Biological Physics*, volume 1, pages 403–463. Elsevier, 1995.

[SZHZ20] Qing Shao, Shaodong Zhang, Zhen Hu, and Yongfeng Zhou. Multimode Self-Oscillating Vesicle Transformers. *Angew.Chem*, 59:17125 – 17129, 2020.

[TN20] Naoki Tamemoto and Hiroshi Noguchi. Pattern formation in reaction–diffusion system on membrane with mechanochemical feedback. *Scientific reports*, 10(19582), 2020.

[TN21] Naoki Tamemoto and Hiroshi Noguchi. Reaction-diffusion waves coupled with membrane curvature. *Soft Matter*, 17(6589–6596), 2021.

[TN22] Naoki Tamemoto and Hiroshi Noguchi. Excitable reaction-diffusion waves of curvature-inducing proteins on deformable membrane tubes. *Phys.Rev.E*, 106(024403), 2022.

[TUSY14] Ryota Tamate, Takeshi Ueki, Mitsuhiro Shibayama, and Ryo Yoshida. Self-Oscillating Vesicles: Spontaneous Cyclic Structural Changes of Synthetic Diblock Copolymers. *Angew.Chem*, 53:11248–11252, 2014.

[Uec21] H. Uecker. *Numerical continuation and bifurcation in Nonlinear PDEs*. SIAM, Philadelphia, PA, 2021.

[YFB22] A. Yochelis, S. Flemming, and C. Beta. Versatile patterns in the actin cortex of motile cells: Self-organized pulses can coexist with macropinocytic ring-shaped waves. *Phys.Rev.Letters*, 129:088101, 2022.

[ZHL17] S. Zhao, T. Healey, and Q. Li. Direct computation of two-phase icosahedral equilibria of lipid bilayer vesicles. *Comput. Methods Appl. Mech. Engrg.*, 314:164–179, 2017.